

# Superconductivity and non-Fermi liquid behavior near a nematic quantum critical point

Samuel Lederer,<sup>1</sup> Yoni Schattner,<sup>2</sup> Erez Berg,<sup>2</sup> and Steven A. Kivelson<sup>3</sup>

<sup>1</sup>*Department of Physics, Massachusetts Institute of Technology, Cambridge, MA 02139, USA*

<sup>2</sup>*Department of Condensed Matter Physics, The Weizmann Institute of Science, Rehovot, 76100, Israel*

<sup>3</sup>*Department of Physics, Stanford University, Stanford, CA 94305, USA*

(Dated: March 8, 2017)

Using determinantal quantum Monte Carlo, we compute the properties of a lattice model with spin  $\frac{1}{2}$  itinerant electrons tuned through a quantum phase transition to an Ising nematic phase. The nematic fluctuations induce superconductivity with a broad dome in the superconducting  $T_c$  enclosing the nematic quantum critical point. For temperatures above  $T_c$ , we see strikingly non-Fermi liquid behavior, including a “nodal - anti nodal dichotomy” reminiscent of that seen in several transition metal oxides. In addition, the critical fluctuations have a strong effect on the low frequency optical conductivity, resulting in behavior consistent with “bad metal” phenomenology.

Upon approach to a quantum critical point (QCP), the correlation length,  $\xi$ , associated with order parameter fluctuations diverges; consequently microscopic aspects of the physics are averaged out and certain properties of the system are universal. Asymptotically close to criticality, *exact* theoretical predictions concerning the scaling behavior of some measurable quantities are possible. However, in solids, it is rarely possible to convincingly access asymptopia; there are few experimentally documented cases in which a thermodynamic susceptibility grows as a function of decreasing temperature,  $T$ , in proportion to a single power law  $\chi \sim T^{-x}$  over significantly more than one decade of magnitude. This is particularly true of metallic QCPs, where the metallic critical point may be preempted by the occurrence of a superconducting dome, a fluctuation driven first order transition, or some other catastrophe.

However, there is a looser sense in which a QCP can serve as an organizing principle for understanding properties of solids over a range of parameters: In the “neighborhood” of a QCP, where  $\chi$  is large (in natural units) and  $\xi$  is more than a few lattice constants, it is reasonable to conjecture that quantum critical fluctuations play a significant role in determining the properties of the material and that, at least on a qualitative level, those properties may be robust (*i.e.* not strongly dependent on microscopic details), even if they are not universal.

With this in mind, we have carried out extensive numerical “experiments” on a simple 2D lattice model of itinerant electrons coupled to an Ising-like “nematic” order parameter field, Eq. 1. By varying a parameter in the Hamiltonian,  $h$ , the system can be tuned through a quantum or thermal transition from a disordered (symmetric) phase to a nematic phase that spontaneously breaks the lattice symmetry from  $C_4$  to  $C_2$ . Related models of nematic quantum criticality have been studied extensively [1–27] using various analytic methods, and can also be studied with minus-sign-free determinantal quantum Monte Carlo (DQMC) [28–30]. Moreover, the model is

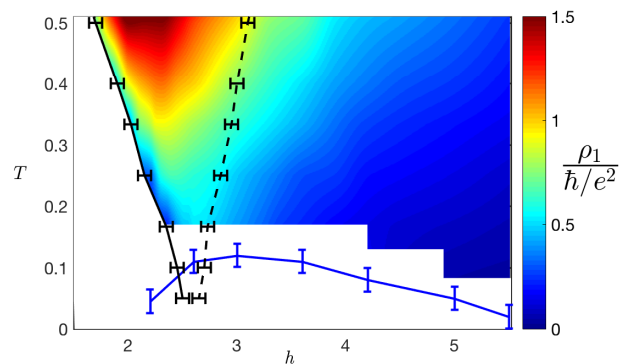


FIG. 1. Phase diagram as a function of the transverse field  $h$  and temperature  $T$ , both measured in units of the fermion hopping  $t$ . The solid and dashed black lines indicate, respectively, the boundary of the nematic phase ( $T_{nem}$ ) and a crossover ( $T_{nem}^*$ , defined shortly before (2)) marking the edge of the quantum critical fan. The superconducting  $T_c$  is indicated by the blue solid line. The color scale shows a proxy for the DC resistivity in units of  $\hbar/e^2$ , defined from the fit in (4). Here,  $\alpha = 1.5$ ,  $V = 0.5t$ ,  $\mu = t$ . Error bars reflect finite size errors, as described in the Supplement.

particularly topical, as there is good evidence that a nematic QCP underlies the superconducting dome in many (possibly all) of the Fe-based superconductors [31–37] and possibly even the cuprate high temperature superconductors [38–40]. This prospect has recently been explored using Monte Carlo methods in [41–44].

In a previous study [41] of this model, we focused on the critical scaling at the putative metallic QCP with a moderate dimensionless coupling between the itinerant electrons and the nematic fluctuations  $\alpha = 1/2$ . We found that, though superconducting fluctuations are enhanced when the tuning parameter  $h$  is close to the quantum critical value,  $h_c$ , the superconducting  $T_c$  (if any) is below the accessible range of temperatures. We documented a possible mild breakdown of Fermi liquid behav-

ior, and identified a broad range of small  $T$  and  $|h - h_c|$  in which some correlation functions are well approximated by simple scaling functions. However, other correlations with the same symmetries do not exhibit the same scaling behavior. This implies that the regime we accessed is far enough from criticality that corrections to scaling are significant, or that the scaling behavior we see does not reflect the properties of a metallic QCP at all.

In the present paper, we have focused on the properties of the model in the critical “neighborhood,” and have taken larger values of  $\alpha = 1 - 1.5$  so that all the energy scales are enhanced, making them easier to document in numerical experiments. Our principal findings are:

1) As shown in Fig. 1, there is a broad superconducting dome with its  $T_c$  maximum roughly coincident with the value  $h = h_c$  at which the nematic transition temperature,  $T_{nem} \rightarrow 0$ . The maximum  $T_c$  is found to be about  $0.03E_F$ , where  $E_F$  is the Fermi energy.

2) Fig. 2 shows the electron spectral function,  $A(\vec{k}, \omega)$ , integrated over a range of energies of order  $T$  about the Fermi energy, as defined in Eq. 2. The nematic fluctuations are exceedingly effective in destroying quasiparticles, and indeed produce a striking “nodal - anti nodal” dichotomy in which some remnant of the Fermi surface is still visible along the zone diagonal. This is associated with the existence of “cold-spots” [45, 46] on the Fermi surface that are required by symmetry. Away from the cold-spots, the imaginary part of the (Matsubara) self energy, shown in Fig. 3, is dramatically unlike that of a Fermi liquid throughout the quantum critical regime.

3) Transport properties are also strongly affected in the quantum critical regime above  $T_c$ . Since analytic continuation of imaginary time data to real time is numerically ill-posed, we have carried out two different procedures to obtain *proxies* for the resistivity. These proxies, plotted in Fig. 5, track the DC resistivity under certain assumptions described below. The first proxy,  $\rho_1$ , is derived from a simple two-component fit to the DQMC data (shown in Fig. 4) while the second,  $\rho_2$ , defined in Eq. 7, is extracted directly from the long (imaginary) time behavior of the current-current correlation function. The results obtained by the two methods are qualitatively similar. At  $h = h_c$  both proxies are roughly linearly increasing functions of  $T$ . For the larger value of the coupling constant, the proxies exceed the quantum of resistance,  $\rho_q = \hbar/e^2$ , at high temperatures (but still much below  $E_F$ ). Outside the quantum critical fan, the proxies are substantially smaller than  $\rho_q$  for all  $T$ . (See also Fig. 1.)

## THE MODEL

Our model is defined on a two-dimensional square lattice, where every site has a single Wannier orbital. Each link has a pseudospin-1/2 degree of freedom that couples

to the fermion bond-density. The system is described by the Hamiltonian

$$\begin{aligned} H &= H_f + H_b + H_{\text{int}}, \\ H_f &= -t \sum_{\langle i,j \rangle, \sigma} c_{i\sigma}^\dagger c_{j\sigma} - \mu \sum_{i, \sigma} c_{i\sigma}^\dagger c_{i\sigma}, \\ H_b &= V \sum_{\langle\langle i,j \rangle\rangle; \langle\langle k,l \rangle\rangle} \tau_{i,j}^z \tau_{k,l}^z - h \sum_{\langle i,j \rangle} \tau_{i,j}^x, \\ H_{\text{int}} &= \alpha t \sum_{\langle i,j \rangle, \sigma} \tau_{i,j}^z c_{i\sigma}^\dagger c_{j\sigma}, \end{aligned} \quad (1)$$

where  $c_{j\sigma}^\dagger$  creates a fermion on site  $j$  with spin  $\sigma = \uparrow, \downarrow$ ,  $\langle i, j \rangle$  denotes a pair of nearest-neighbor sites,  $t$  and  $\mu$  are the hopping strength and chemical potential, respectively,  $\tau_{i,j}^a$  ( $a = x, y, z$ ) denote pseudospin 1/2 operators that live on the bond connecting the neighboring sites  $i$  and  $j$ ,  $V > 0$  is the Ising interaction between nearest-neighbor pseudospins (here,  $\langle\langle i, j \rangle\rangle; \langle\langle k, l \rangle\rangle$  denotes a pair of nearest-neighbor bonds),  $h$  is the strength of a transverse field that acts on the pseudospins, and  $\alpha$  is the dimensionless coupling strength between the pseudospin and the fermion bond density. In the ordered phase where  $V$  dominates,  $\tau_{i,j}^z$  adopts a staggered configuration, taking different values on horizontal and vertical bonds, thereby generating nematic order.

## DQMC RESULTS

A typical phase diagram is shown in Fig. 1, for  $\alpha = 1.5, V = 0.5t, \mu = t$ . [47] (Hereafter, we use units in which  $t = \hbar = e^2 = 1$ ). In addition to the nematic and symmetric phases, there is a “dome” of superconductivity with maximum critical temperature near  $h_c$ , as anticipated [3, 11, 15, 48]. The pair wave-function in the superconducting state has spin singlet s-wave symmetry in the symmetric phase and mixed s and d-wave symmetry in the nematic phase.

The boundary of the nematic phase  $T_{nem}$  and the crossover temperature  $T_{nem}^*$  are both derived from an analysis of the thermodynamic nematic susceptibility  $\chi(h, T) \equiv \frac{1}{L^2} \sum_{i,j} \int_0^\beta d\tau \langle N_i(\tau) N_j(0) \rangle$ , where the nematic order parameter is defined as  $N_i = \sum_j \eta_{ij} \tau_{i,j}^z$ , where  $\eta$  is a d-wave form factor:  $\eta_{ij} = 1/4$  for  $\mathbf{r}_{ij} = \pm \hat{\mathbf{x}}$ ,  $\eta_{ij} = -1/4$  for  $\mathbf{r}_{ij} = \pm \hat{\mathbf{y}}$ , and  $\eta_{ij} = 0$  otherwise.  $T_{nem}$  is determined using finite size scaling appropriate to a two-dimensional classical Ising transition, while  $T_{nem}^*(h)$  is defined implicitly according to  $\chi(h, T_{nem}^*) = \frac{1}{2} \chi(h_c, T_{nem}^*)$ . The superconducting critical temperature  $T_c$  is determined by analysis of the superfluid stiffness [49, 50], and can also be estimated by other methods, yielding similar results [51].

The presence of superconductivity limits the region in which any scaling behavior of nematic fluctuations can be identified. That said, for temperatures well above  $T_c$ , the thermodynamic nematic susceptibility near  $h_c$  is

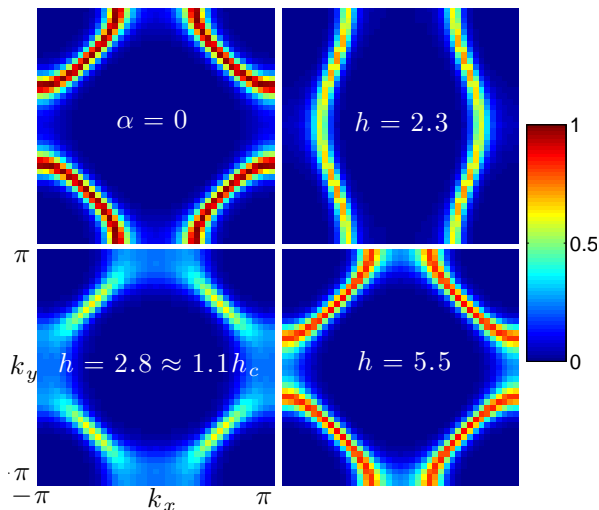


FIG. 2. The low frequency fermionic spectral weight  $\mathcal{G}(\vec{k})$  [Eq. (2)] at temperature  $T = 0.17$ , shown for the noninteracting band structure ( $\alpha = 0$ ), and for  $\alpha = 1.5$  for several values of  $h$ . For  $h = 2.3$ , a small  $C_4$  symmetry-breaking field has been applied in the simulation. Data are for a  $20 \times 20$  system with various combinations of periodic and antiperiodic boundary conditions. Other parameters are  $V = 0.5$  and,  $\mu = 1.0$ .

similar in structure to that reported in [41]. Nematic fluctuations at nonzero frequency have somewhat different structure than those previously reported, and have a reduced dependence on momentum.

Turning to single-particle properties, we examine [52]

$$\mathcal{G}(\vec{k}) \equiv 2\tilde{G}\left(\vec{k}, \tau = \frac{\beta}{2}\right) = \int d\omega \frac{A(\vec{k}, \omega)}{\cosh[\beta\omega/2]} \quad (2)$$

where  $\tilde{G}$  is the imaginary time fermion Green function and  $A$  is the real frequency spectral function. Roughly,  $\mathcal{G}$  measures spectral weight within an energy range of order  $T$  of the Fermi level, so that a sharp peak in the momentum dependence of  $\mathcal{G}$  indicates an underlying Fermi surface. In a Fermi liquid,  $\mathcal{G}(\vec{k})$  is peaked at the Fermi surface with a peak amplitude that approaches the quasi-particle residue  $Z_{\vec{k}}$  as  $T \rightarrow 0$ .

Fig. 2 shows color plots of  $\mathcal{G}$  at fixed temperature  $T = 0.17$  for the non-interacting case ( $\alpha = 0$ ) and for  $\alpha = 1.5$  at a variety of values of  $h$ . For  $h = 5.5$ , deep in the symmetric phase, there is a clear Fermi surface similar to that of the non-interacting problem. For  $h = 2.3$ , in the ordered phase, there is also a clear Fermi surface consisting of open sheets, reflecting a substantial nematic distortion. For  $h = 2.8$ , near  $h_c$ , a Fermi surface appears well-defined near the cold spots along the zone diagonal, but is increasingly ill-defined away from these high-symmetry points. The higher degree of coherence along the zone diagonal is expected by symmetry: long-wavelength nematic fluctuations cannot couple to fermions with momentum along the zone diagonal.

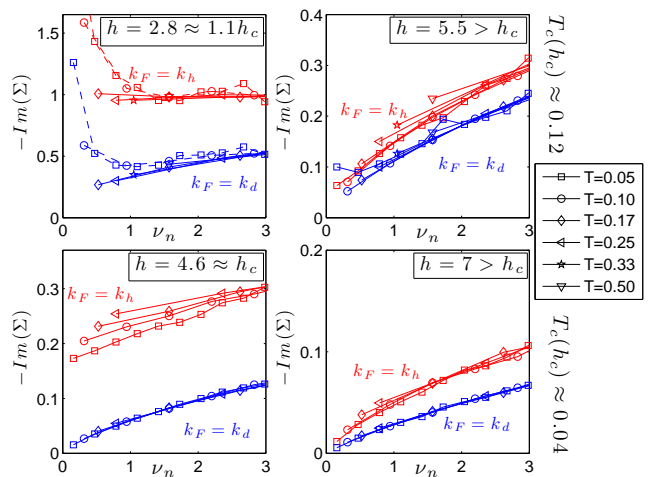


FIG. 3. The imaginary part of the fermion self-energy for two values of parameters:  $\alpha = 1.5, V = 0.5, \mu = 1.0$  (top row), and  $\alpha = 1.0, V = 1.0, \mu = 0.5$  (bottom row), for various temperatures, and with the nominal Fermi momenta  $\vec{k}_d$  and  $\vec{k}_h$  along the  $(0, 0) - (\pi, \pi)$  and  $(0, \pi) - (\pi, \pi)$  directions, respectively. Data are shown for a  $20 \times 20$  system both near  $h_c$  (left column) and far in the symmetric phase (right column). In the upper left panel, data points below  $T_c$  are connected by dashed lines.

A complementary probe of single fermion properties is the self energy, extracted from the Green function  $G(\vec{k}, \nu_n)$  and the non-interacting Green function  $G_0(\vec{k}, \nu_n)$  according to  $\Sigma(\vec{k}, \nu_n) \equiv G_0^{-1}(\vec{k}, \nu_n) - G^{-1}(\vec{k}, \nu_n)$ . (Henceforth,  $\nu_n = 2\pi T(n + 1/2)$  and  $\omega_n = 2\pi Tn$  will designate the fermionic and bosonic Matsubara frequencies.) In a Fermi liquid at asymptotically low temperature,  $-\text{Im}[\Sigma(\vec{k}_F, \nu_n)] = \gamma_{\vec{k}} + (1/Z_{\vec{k}} - 1)\nu_n + \mathcal{O}(\nu_n^2)$  for  $\nu_n > 0$ , where  $\gamma_{\vec{k}}(T) \ll T$  is the inelastic scattering rate. More generally,  $\gamma_{\vec{k}}$  is obtained by extrapolating  $-\text{Im}[\Sigma]$  to zero frequency. In Fig. 3 we plot  $-\text{Im}[\Sigma(\vec{k}, \nu_n)]$  vs.  $\nu_n$ , both close to  $h_c$  and deep in the disordered phase. We show data for a variety of temperatures for  $\vec{k}$  at the nominal Fermi momenta  $\vec{k}_d$  and  $\vec{k}_h$  along the  $(0, 0) - (\pi, \pi)$  and  $(0, \pi) - (\pi, \pi)$  directions, respectively.

In the disordered phase, the frequency and temperature dependences of  $\text{Im}[\Sigma]$  at both  $\vec{k}_d$  and  $\vec{k}_h$  are consistent with Fermi liquid theory – the extrapolated  $\nu_n \rightarrow 0$  intercept ( $\gamma_{\vec{k}}$ ) is well below  $T$  and the slope is finite (corresponding to  $1 > Z_{\vec{k}} > 0$ ) and hardly  $T$  dependent. Even for  $h \approx h_c$ , Fermi liquid theory is loosely consistent with the data at  $\vec{k}_d$ , but not remotely so at  $\vec{k}_h$  where  $\gamma_{\vec{k}_h}$  exceeds  $T$ , and appears not to vanish in the  $T \rightarrow 0$  limit. In the quantum critical regime and above  $T_c$ , quasiparticles far from the cold spots are not even marginally well-defined. (The upturn of  $\text{Im}[\Sigma]$  at low frequency, visible especially for  $\alpha = 1.5$ , is associated with the onset of a superconducting gap.)

The intervention of superconductivity complicates any

analysis of the putative low temperature Fermi liquid properties as  $h \rightarrow h_c$ . However, to obtain a rough sense of trends, one can estimate the dispersion of the quasiparticle-like features as a function of  $h$  and  $T$  at different parts of the Fermi surface (see Supplementary Information for details). We see a tendency for the dispersion to become substantially flatter as  $h \rightarrow h_c$  (*i.e.* a large increase in the “effective mass”), though any such renormalization is much weaker or non-existent at the cold spots on the Fermi surface. The electronic spectral function  $A(\vec{k}, \omega)$ , calculated from  $G(\vec{k}, \nu_n)$  using the maximum entropy method, is consistent with such behavior (see Supplementary Information). Near the cold spots  $A(\vec{k}, \omega)$  has a well-defined dispersive peak, while in the hot regions at  $h \approx h_c$  there are only broad features without a clear dispersion. Below the superconducting  $T_c$ ,  $A(\vec{k}, \omega)$  clearly displays a superconducting gap in both the cold spots and the hot regions (with a larger gap in the hot regions).

The breakdown of Fermi liquid theory seen in the fermion Green function suggests that transport properties may also be strongly altered near the QCP. One quantity of great interest is the DC conductivity, but the DC limit of transport is particularly difficult to access using analytic continuation of imaginary time data. The analysis we carry out below yields information about the optical conductivity at frequencies of order the temperature, but any statements about the DC conductivity rest on additional, nontrivial assumptions.

We have measured the imaginary time ordered current-current correlator  $\tilde{\Lambda}_{ii}(\tau) \equiv \langle T J_i(\tau) J_i(0) \rangle$ , where  $J_i$  is the uniform current operator in direction  $i = x$  or  $y$ . (We will henceforth leave the directional indices implicit.)  $\Lambda(\omega_n)$ , the Fourier transform of  $\tilde{\Lambda}(\tau)$ , is shown in Fig. 4a for  $\alpha = 1.5, V = 0.5, \mu = 1, h \approx h_c$ , &  $T = 0.17 \approx 1.5T_c$ . In a non-superconducting state,  $\Lambda(\omega_n)$  is related to the real part of the optical conductivity  $\sigma'(\omega)$  by

$$\Lambda(\omega_n) = \int \frac{d\omega}{\pi} \frac{\omega^2 \sigma'(\omega)}{\omega^2 + \omega_n^2}. \quad (3)$$

A clear feature, present throughout the non-superconducting portions of the phase diagram, is a substantial jump in  $\Lambda(\omega_n)$  between the zeroth and first Matsubara frequency. This is evidence of a Drude-like component of  $\sigma'(\omega)$  peaked at low frequencies, with a width less than or comparable to  $T$ . The slow decrease of  $\Lambda(\omega_n)$  for  $n > 1$  is indicative of an additional broad feature with optical weight spread over a range of frequencies large compared to  $T$ .

We have performed a simple analytic continuation of our data via a least squares fit. The fitting function is a sum of two terms [53]

$$\Lambda_{\text{fit}}(\omega_n) = \sum_{j=1}^2 \frac{A_j}{\omega_n^2 + \gamma_j |\omega_n| + \Omega_j^2}. \quad (4)$$

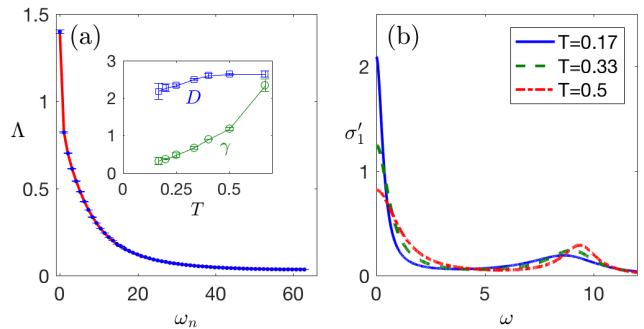


FIG. 4. Left: the current-current correlator for a  $16 \times 16$  system with  $h = 2.6 \approx h_c, T = 0.17$ , for  $\alpha = 1.5, V = 0.5, \mu = 1$ . Error bars are comparable to the symbol size. The solid red line is a least-squares fit to two components of the form of (4). Right: the corresponding real part of the optical conductivity for parameters on the left, as well as two higher temperatures, showing how the Drude-like peak sharpens on cooling. The temperature dependence of the half-width at half-maximum  $\Gamma$  of the Drude-like peak, as well as its weight  $D$ , are shown in the inset to the left panel, with error bars estimated as described in the supplement.

$\Lambda_{\text{fit}}$  can then be analytically continued to give

$$\sigma'(\omega) = \sum_{j=1}^2 \frac{A_j \gamma_j}{(\Omega_j^2 - \omega^2)^2 + \gamma_j^2 \omega^2}. \quad (5)$$

As illustrated in Fig. 4a, the fit agrees with the data within a few percent. The corresponding optical conductivity is shown in Fig. 4b for a variety of temperatures above  $T_c$ ; it consists of a Drude-like component with its maximum at  $\omega = 0$  (*i.e.*  $\gamma_1 > \sqrt{2}\Omega_1$ ) that broadens with increasing temperature, and a broad, largely temperature-independent background with a maximum at  $\omega = \sqrt{|\Omega_2|^2 - |\gamma_2|^2}/2} > 0$ . The zero frequency limit of this fitted conductivity yields a proxy  $\rho_1$  for the DC resistivity.

Though physically plausible and in agreement with our data, the fitting analysis is not unique – analytic continuation of numerical data is a famously ill-conditioned problem [54]. As one check on our results, we have performed the analytic continuation using standard maximum entropy methods; the results, as shown in the Supplementary Material, are very similar to those obtained above. On the other hand, as also shown in the Supplementary Material, the quality of the fit is similar if we mandate a third component with width far less than the temperature, which would of course drastically alter the DC conductivity. Such a narrow peak may arise if there is an emergent nearly-conserved momentum [23, 55].

Analysis of the current-current correlator in the time domain yields additional information. The value and the derivatives of  $\tilde{\Lambda}(\tau)$  near  $\tau = \beta/2$  contain information about the moments of the low frequency part of the op-



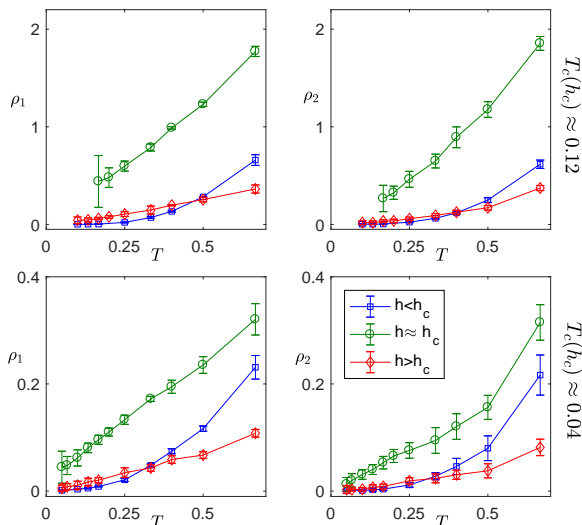


FIG. 5. The temperature dependence of the resistivity proxies (in units of  $\hbar/e^2$ ) for parameters  $\alpha = 1.5, V = 0.5, \mu = 1$  (top row, for  $h = 2.0 < h_c$ ,  $h = 2.6 \approx h_c$  and  $h = 5.5 > h_c$ ) and  $\alpha = 1.0, V = 1.0, \mu = 0.5$  (bottom row, for  $h = 4.0 < h_c$ ,  $h = 4.6 \approx h_c$  and  $h = 7.0 > h_c$ ). For  $h < h_c$ , a small symmetry breaking field has been applied, and the smaller component of the resistivity proxy is shown. Values shown are for the largest system size simulated ( $L = 16$  or  $18$  depending on temperature), with error bars estimated as described in the Supplementary Material.

tical conductivity:

$$[\partial_\tau^{2m} \tilde{\Lambda}]_{\tau=\beta/2} = \int \frac{d\omega}{2\pi} \frac{\omega^{2m+1} \sigma'(\omega)}{\sinh\left(\frac{\beta\omega}{2}\right)}. \quad (6)$$

The first two such moments obtained from our QMC simulations are shown in the Supplementary Material. (Interestingly, these moments can also be straightforwardly computed from empirical data, enabling direct comparison with experiment.)

The two lowest order moments can be combined into a quantity with units of resistivity according to

$$\rho_2 \equiv [\partial_\tau^2 \tilde{\Lambda} / (2\pi \tilde{\Lambda}^2)]_{\tau=\beta/2}. \quad (7)$$

This quantity tracks the DC resistivity at low temperatures whenever the low frequency ( $\omega \lesssim T$ ) conductivity can be described by a single Drude-like component which either has Lorentzian shape or a width of order  $T$ . This is a parsimonious (although not unassailable) assumption and consistent with our data. With caveats in place, we now describe the behavior of the two resistivity proxies  $\rho_{1,2}$  defined above.

$\rho_1(h, T)$  is represented in the coloring of the symmetric metallic region of the phase diagram in Fig. 1. It exhibits a non-monotonic dependence on  $h$ , with a maximum near  $h_c$ . The temperature dependence of  $\rho_1$  and  $\rho_2$  are shown in Fig. 5 in the ordered and disordered phases

as well as at  $h_c$ , for both  $\alpha = 1.5, V = 0.5, \mu = 1.0$  and  $\alpha = 1.0, V = 1.0, \mu = 0.5$ .  $\rho_1$  and  $\rho_2$  are qualitatively similar over a wide range of temperatures. Both are significantly higher at  $h \approx h_c$  than deep in the ordered and disordered phases. In the ordered phase, the data are roughly consistent with the  $T^2$  temperature dependence expected of a Fermi liquid. In the disordered phase, the temperature dependence in the range of  $T > T_c$  can be fit to a linear function of  $T$  with small slope and a slightly negative extrapolated value at  $T \rightarrow 0$ . [56]

At  $h \approx h_c$ , the behavior depends somewhat on parameters. For  $\alpha = 1.0, V = 1.0, \mu = 0.5$ , there is an apparent  $T$ -linear behavior over about a decade of temperature. For  $\alpha = 1.5, V = 0.5, \mu = 1.0$ , the high  $T_c$  leaves an insufficient dynamical range to establish a clear power law temperature dependence, but both  $\rho_1$  and  $\rho_2$  exceed the Ioffe-Regel limit of  $\hbar/e^2$  at a temperature of approximately  $3T_c$ . Subject always to the uncertainties in analytic continuation, the behavior of our model near  $h_c$  is strikingly reminiscent of the “bad metal” phenomenology seen in many correlated materials [57–59].

We have performed additional simulations at lower fermionic densities, with results summarized in the supplementary material. Much of the phenomenology appears to be robust: Close to  $h_c$ , the imaginary part of the fermionic self-energy at  $\vec{k}_h$  approaches a constant and the resistivity is of order of the quantum of resistance. However, the temperature dependence of the resistivity is not linear. Also, for certain values of the couplings, we find evidence that the nematic transition becomes weakly first order at low temperatures.

## DISCUSSION

We have studied the vicinity of a nematic QCP in a simple lattice model of a metal. The QCP is masked by a dome-shaped superconducting phase. The normal-state quantum critical regime does not exhibit clear scaling behavior; however, it displays strong anomalies that we associate with the approach to the QCP. In particular, the fermion self-energy is strikingly non-Fermi liquid like over much of the Fermi surface. The optical conductivity at frequencies  $\lesssim T$  is also strongly affected by the critical fluctuations. Assuming a simple form of  $\sigma(\omega)$ , we find that the DC resistivity is anomalously large (exceeding the Ioffe-Regel limit for  $\alpha > 1$ ) and nearly linear in temperature.

While our model does not accurately describe the microscopics of any specific material, and ignores physical effects that may be important [60–63], it is plausible that the qualitative behavior proximate to the QCP is relatively insensitive to microscopic details. Our results bear striking similarities to the behavior seen in certain high temperature superconductors: in several iron-based superconductors, the resistivity is anomalously large and

$T$ -linear near the putative nematic QCP [32, 64], and the fermionic spectral properties of our model in the critical regime are reminiscent of the “nodal-antinodal dichotomy” reported in the “strange metal” regime of certain cuprates [65, 66].

*Acknowledgements.*— S. L. and Y. S. have contributed equally to this work. The authors acknowledge fruitful discussions with Andrey Chubukov, Snir Gazit, Sean Hartnoll, Mohit Randeria, Subir Sachdev, Boris Spivak, and Yochai Werman. S. L. was supported by a Gordon and Betty Moore Post Doctoral Fellowship at MIT. S. A. K. was supported in part by NSF grant DMR 1265593 at Stanford. Y. S. and E. B. were supported by the Israel Science Foundation under Grant No. 1291/12, by the US-Israel BSF under Grant No. 2014209, and by a Marie Curie reintegration grant. E. B. was supported by an Alon fellowship. This work was performed in part at the Aspen Center for Physics, which is supported by National Science Foundation grant PHY-1066293.

- 
- [1] V. Oganesyan, S. A. Kivelson, and E. Fradkin, *Phys. Rev. B* **64**, 195109 (2001).
- [2] W. Metzner, D. Rohe, and S. Andergassen, *Phys. Rev. Lett.* **91**, 066402 (2003).
- [3] Y. B. Kim and H.-Y. Kee, *Journal of Physics: Condensed Matter* **16**, 3139 (2004).
- [4] L. Dell’Anna and W. Metzner, *Phys. Rev. B* **73**, 045127 (2006).
- [5] M. J. Lawler, D. G. Barci, V. Fernández, E. Fradkin, and L. Oxman, *Phys. Rev. B* **73**, 085101 (2006).
- [6] M. Metlitski and S. Sachdev, *Physical Review B* **82**, 075127 (2010).
- [7] D. F. Mross, J. McGreevy, H. Liu, and T. Senthil, *Physical Review B* **82**, 045121 (2010).
- [8] D. L. Maslov and A. V. Chubukov, *Phys. Rev. B* **81**, 045110 (2010).
- [9] A. L. Fitzpatrick, S. Kachru, J. Kaplan, and S. Raghu, *Phys. Rev. B* **88**, 125116 (2013).
- [10] D. Dalidovich and S.-S. Lee, *Phys. Rev. B* **88**, 245106 (2013).
- [11] M. A. Metlitski, D. F. Mross, S. Sachdev, and T. Senthil, *Physical Review B* **91**, 115111 (2015).
- [12] T. Holder and W. Metzner, *Phys. Rev. B* **92**, 041112 (2015), [arXiv:1503.05089 \[cond-mat.str-el\]](https://arxiv.org/abs/1503.05089).
- [13] S. C. Thier and W. Metzner, *Phys. Rev. B* **84**, 155133 (2011).
- [14] I. Mandal and S.-S. Lee, *Phys. Rev. B* **92**, 035141 (2015).
- [15] S. Lederer, Y. Schattner, E. Berg, and S. A. Kivelson, *Phys. Rev. Lett.* **114**, 097001 (2015).
- [16] A. Eberlein, I. Mandal, and S. Sachdev, *Phys. Rev. B* **94**, 045133 (2016).
- [17] I. Mandal, *Phys. Rev. B* **94**, 115138 (2016).
- [18] I. Mandal, (2016), [arXiv:1608.06642](https://arxiv.org/abs/1608.06642).
- [19] A. A. Patel, A. Eberlein, and S. Sachdev, (2016), [arXiv:1607.03894](https://arxiv.org/abs/1607.03894).
- [20] M. Punk, *Phys. Rev. B* **94**, 195113 (2016).
- [21] S. A. Hartnoll, R. Mahajan, M. Punk, and S. Sachdev, *Phys. Rev. B* **89**, 155130 (2014).
- [22] C. Drukier, L. Bartosch, A. Isidori, and P. Kopietz, *Phys. Rev. B* **85**, 245120 (2012).
- [23] R. Mahajan, D. M. Ramirez, S. Kachru, and S. Raghu, *Phys. Rev. B* **88**, 115116 (2013).
- [24] A. L. Fitzpatrick, S. Kachru, J. Kaplan, and S. Raghu, *Phys. Rev. B* **89**, 165114 (2014).
- [25] S. Raghu, G. Torroba, and H. Wang, *Phys. Rev. B* **92**, 205104 (2015).
- [26] T. Holder and W. Metzner, *Phys. Rev. B* **92**, 245128 (2015).
- [27] B. Meszner, P. Sätterskog, A. Bagrov, and K. Schalm, *Phys. Rev. B* **94**, 115134 (2016).
- [28] R. Blankenbecler, D. J. Scalapino, and R. L. Sugar, *Physical Review D* **24**, 2278 (1981).
- [29] R. T. Scalettar, E. Y. Loh, J. E. Gubernatis, A. Moreo, S. R. White, D. J. Scalapino, R. L. Sugar, and E. Dagotto, *Phys. Rev. Lett.* **62**, 1407 (1989).
- [30] F. F. Assaad, in *Quantum Simulations Complex Many-Body Syst. From Theory to Algorithms*, John von Neumann Institute for Computing (NIC) Series, Vol. 10, edited by J. Grotendorst, D. Marx, and A. Muramatsu (FZ-Jülich, Jülich, Germany, 2002).
- [31] C.-L. Song, Y.-L. Wang, P. Cheng, Y.-P. Jiang, W. Li, T. Zhang, Z. Li, K. He, L. Wang, J.-F. Jia, *et al.*, *Science* **332**, 1410 (2011).
- [32] J.-H. Chu, H.-H. Kuo, J. G. Analytis, and I. R. Fisher, *Science* **337**, 710 (2012), [arXiv:1203.3239 \[cond-mat.supr-con\]](https://arxiv.org/abs/1203.3239).
- [33] Y. Gallais, R. M. Fernandes, I. Paul, L. Chauvière, Y.-X. Yang, M.-A. Méasson, M. Cazayous, A. Sacuto, D. Colson, and A. Forget, *Phys. Rev. Lett.* **111**, 267001 (2013).
- [34] R. Zhou, Z. Li, J. Yang, D. Sun, C. Lin, and G.-q. Zheng, *Nature Communications* **4**, 2265 (2013).
- [35] A. E. Böhrer, P. Burger, F. Hardy, T. Wolf, P. Schweiss, R. Fromknecht, M. Reinecker, W. Schranz, and C. Meingast, *Physical Review Letters* **112**, 047001 (2014), [arXiv:1305.3515 \[cond-mat.supr-con\]](https://arxiv.org/abs/1305.3515).
- [36] V. K. Thorsmølle, M. Khodas, Z. P. Yin, C. Zhang, S. V. Carr, P. Dai, and G. Blumberg, *Phys. Rev. B* **93**, 054515 (2016).
- [37] H.-H. Kuo, J.-H. Chu, J. C. Palmstrom, S. A. Kivelson, and I. R. Fisher, *Science* **352**, 958 (2016).
- [38] D. Haug, V. Hinkov, A. Suchaneck, D. Inosov, N. B. Christensen, C. Niedermayer, P. Bourges, Y. Sidis, J. T. Park, A. Ivanov, C. T. Lin, J. Mesot, and B. Keimer, *Phys. Rev. Lett.* **103**, 017001 (2009).
- [39] R. Daou, J. Chang, D. LeBoeuf, O. Cyr-Choinière, F. Laliberté, N. Doiron-Leyraud, B. J. Ramshaw, R. Liang, D. A. Bonn, W. N. Hardy, and L. Taillefer, *Nature* **463**, 519 (2010).
- [40] M. Lawler, K. Fujita, J. Lee, A. Schmidt, Y. Kohsaka, C. K. Kim, H. Eisaki, S. Uchida, J. Davis, J. Sethna, *et al.*, *Nature* **466**, 347 (2010).
- [41] Y. Schattner, S. Lederer, S. A. Kivelson, and E. Berg, *Physical Review X* **6**, 031028 (2016), [arXiv:1511.03282 \[cond-mat.supr-con\]](https://arxiv.org/abs/1511.03282).
- [42] Z.-X. Li, F. Wang, H. Yao, and D.-H. Lee, (2015), [arXiv:1512.04541](https://arxiv.org/abs/1512.04541).
- [43] P. T. Dumitrescu, M. Serbyn, R. T. Scalettar, and A. Vishwanath, *Phys. Rev. B* **94**, 155127 (2016).
- [44] The closely related problem of an Ising ferromagnet has recently been explored by: X.-Y. Xu, K. Sun, Y. Schattner, E. Berg, and Z.-Y. Meng, in preparation (2016).
- [45] W. Metzner, D. Rohe, and S. Andergassen, *Phys. Rev.*

- Lett. **91**, 066402 (2003).
- [46] K. Lee, S. A. Kivelson, and E.-A. Kim, *Phys. Rev. B* **94**, 014204 (2016), [arXiv:1603.03104 \[cond-mat.supr-con\]](#).
- [47] A value of  $\alpha > 1$  is problematic microscopically, since the effective hopping matrix element along one direction changes sign deep in the ordered phase. However, we view Eq. (1) as an effective model designed to give a nematic QCP, and so do not restrict the value of  $\alpha$ .
- [48] T. A. Maier and D. J. Scalapino, *Phys. Rev. B* **90**, 174510 (2014).
- [49] D. J. Scalapino, S. R. White, and S. Zhang, *Physical Review B* **47**, 7995 (1993).
- [50] T. Paiva, R. R. dos Santos, R. T. Scalettar, and P. J. H. Denteneer, *Phys. Rev. B* **69**, 184501 (2004).
- [51] Further details of the finite size scaling analysis, the resistivity proxy  $\tilde{\rho}$ , the form of the self-energy in the superconducting state, and additional data can be found in the Supplementary Material.
- [52] N. Trivedi and M. Randeria, *Phys. Rev. Lett.* **75**, 312 (1995).
- [53] Eq. (4) must be modified to account for the discretization of imaginary time, as discussed in the Supplementary Material.
- [54] J. Gubernatis, M. Jarrell, R. Silver, and D. Sivia, *Physical Review B* **44**, 6011 (1991).
- [55] D. L. Maslov, V. I. Yudson, and A. V. Chubukov, *Phys. Rev. Lett.* **106**, 106403 (2011).
- [56] Recalling that small resistivities correspond to a sharp Drude-like feature in the resistivity – precisely the sort of feature that is most difficult to capture reliably from imaginary time data – we have not attempted a serious analysis of the apparently non-Fermi liquid character of this last observation.
- [57] V. J. Emery and S. A. Kivelson, *Phys. Rev. Lett.* **74**, 3253 (1995).
- [58] N. E. Hussey, K. Takenaka, and H. Takagi, *Phil. Mag.* **84**, 2847 (2004).
- [59] S. A. Hartnoll, *Nature Physics* **11**, 54 (2015).
- [60] E. W. Carlson, K. A. Dahmen, E. Fradkin, and S. A. Kivelson, *Phys. Rev. Lett.* **96**, 097003 (2006).
- [61] L. Nie, G. Tarjus, and S. A. Kivelson, *Proceedings of the National Academy of Sciences* **111**, 7980 (2014).
- [62] U. Karahasanovic and J. Schmalian, *Phys. Rev. B* **93**, 064520 (2016).
- [63] I. Paul and M. Garst, (2016), [arXiv:1610.06168 \[cond-mat.str-el\]](#).
- [64] P. Walmsley, C. Putzke, L. Malone, I. Guillamon, D. Vignolles, C. Proust, S. Badoux, A. I. Coldea, M. D. Watson, S. Kasahara, Y. Mizukami, T. Shibauchi, Y. Matsuda, and A. Carrington, *Physical Review Letters* **110**, 257002 (2013).
- [65] T. Valla, A. V. Fedorov, P. D. Johnson, Q. Li, G. D. Gu, and N. Koshizuka, *Phys. Rev. Lett.* **85**, 828 (2000).
- [66] X. J. Zhou, T. Yoshida, D.-H. Lee, W. L. Yang, V. Brouet, F. Zhou, W. X. Ti, J. W. Xiong, Z. X. Zhao, T. Sasagawa, T. Kakeshita, H. Eisaki, S. Uchida, A. Fujimori, Z. Hussain, and Z.-X. Shen, *Phys. Rev. Lett.* **92**, 187001 (2004).

**Supplementary Information for:  
“Superconductivity and bad metal behavior near a nematic quantum critical point”**

**S-I. DETERMINATION OF PHASE BOUNDARIES**

The nematic phase boundary has been determined using standard finite size scaling techniques appropriate to a two-dimensional classical Ising transition, as described in the appendix of Ref. 1. The superconducting transition temperature has been determined using the helicity modulus, following Ref. 2:

$$\rho_s = \lim_{q_y \rightarrow 0} \lim_{L \rightarrow \infty} K_{xx}(q_x = 0, q_y) \quad (\text{S1})$$

where

$$K_{xx}(\mathbf{q}) \equiv \frac{1}{4} [\Lambda_{xx}(q_x \rightarrow 0, q_y = 0) - \Lambda_{xx}(\mathbf{q})], \quad (\text{S2})$$

and  $\Lambda_{xx}$  is the current-current correlator

$$\Lambda_{xx}(\mathbf{q}) = \sum_i \int_0^\beta d\tau e^{-i\mathbf{q}\cdot\mathbf{r}_i} \langle J_x(\mathbf{r}_i, \tau) J_x(0, 0) \rangle. \quad (\text{S3})$$

Here, the current density operator is given by  $J_x(\mathbf{r}_i) = \sum_\sigma it(1 + \alpha\tau_{i,j}^z)c_{i\sigma}^\dagger c_{j\sigma} + \text{H.c.}$ , where  $\mathbf{r}_j = \mathbf{r}_i + \hat{x}$ . The  $q \rightarrow 0$  limits above are not strictly well defined for finite size systems, so we use the smallest nonzero momentum  $q = 2\pi/L$  to define a value of  $\rho_s$  in finite size systems. Fig. S1 exhibits curves of  $\rho_s(T)$  for various system sizes, which cross at a temperature near where they attain the BKT jump of  $2T/\pi$ . Rough error bars are determined by inspection.

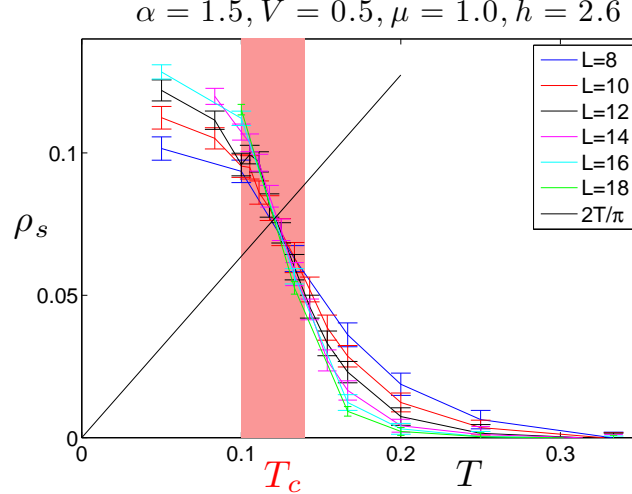


FIG. S1. Helicity modulus versus temperature for various system sizes. The black line represents the BKT jump of  $2T/\pi$ .

The  $T_c$  determined above can be corroborated by examining other thermodynamic quantities (Fig. S-I). For instance the pair susceptibility

$$P_s = \int_0^\beta d\tau \sum_i \langle \Delta_s^\dagger(\mathbf{r}_i, \tau) \Delta_s(0, 0) \rangle. \quad (\text{S4})$$

where,  $\Delta_s(\mathbf{r}_i) = c_{i\uparrow}c_{i\downarrow}$  diverges in the thermodynamic limit only in the superconducting phase. The uniform spin susceptibility also shows evidence of the opening a spin gap in the superconducting phase.



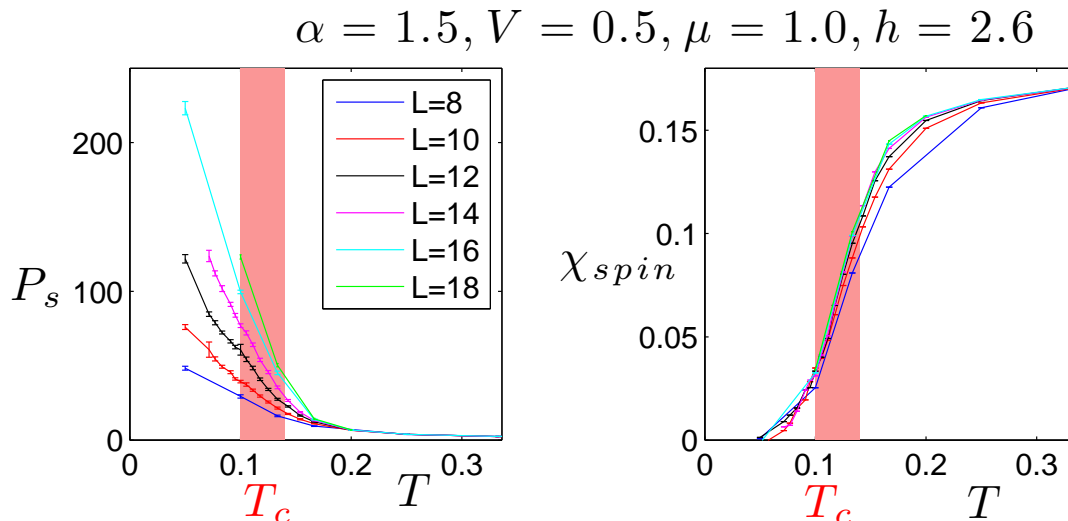


FIG. S2. Left: the onset  $s$ -wave pairing susceptibility versus temperature. Right: the uniform spin susceptibility versus temperature. Both are shown for various system sizes, and indicate a superconducting  $T_c$  consistent with that determined above.

## S-II. ESTIMATING THE DC RESISITIVITY

### A. Resistivity proxy from the long imaginary time data

Next, we describe the “resistivity proxy”  $\rho_2$  introduced in the main text as an estimator for the d.c. resistivity,  $\rho_{dc}$ .  $\rho_2$  can be computed directly from imaginary time data (without the need for any analytical continuation). It is proportional to  $\rho_{dc}$  under certain assumptions, as we discuss below. We have used the resistivity proxy analysis as a complement to direct analytical continuation. The fact that both approaches give a qualitatively similar temperature dependence for the resistivity, and even the quantitative estimates agree within a factor of  $\sim 2$  (see Fig. 5 of the main text), provides support for the validity of our assumptions.

The imaginary-time (and Matsubara frequency) current-current correlations are related to the real part of the real-frequency conductivity by

$$\Lambda(i\omega_n) = \int \frac{d\omega}{\pi} \frac{\omega^2 \sigma'(\omega)}{\omega^2 + \omega_n^2}. \quad (\text{S5})$$

$$\tilde{\Lambda}(\tau) = \int \frac{d\omega}{2\pi} \sigma'(\omega) \frac{\omega \cosh\left[\left(\frac{\beta}{2} - \tau\right)\omega\right]}{\sinh\left(\frac{\beta\omega}{2}\right)}, \quad (\text{S6})$$

[Note that Eq. (S6) is valid for  $0 \leq \tau \leq \beta$ .] Since the kernels in Eqs. (S6,S5) are ill-conditioned, inverting these equations is a highly numerically unstable problem. To make matters worse,  $\sigma'(\omega)$  turns out to have features whose characteristic width is of order  $T$  or less - which is less than the intrinsic “resolution” of the kernel.

However, under many circumstances, we would expect that  $\sigma'(\omega, T)$  at low frequencies is determined by the behavior of  $\tilde{\Lambda}(\tau)$  at the longest imaginary times,  $\tau \sim \beta/2$ , or equivalently by the low-frequency moments (LFMs) [3]

$$m_0 \equiv \beta \tilde{\Lambda}(\tau = \frac{\beta}{2}) = \beta \int \frac{d\omega}{2\pi} \frac{\omega \sigma'(\omega)}{\sinh\left(\frac{\beta\omega}{2}\right)}, \quad (\text{S7})$$

$$m_2 \equiv \beta \partial_\tau^2 \tilde{\Lambda}(\tau = \frac{\beta}{2}) = \beta \int \frac{d\omega}{2\pi} \frac{\omega^3 \sigma'(\omega)}{\sinh\left(\frac{\beta\omega}{2}\right)}, \quad (\text{S8})$$

in terms of which the resistivity proxy defined in the text is

$$\rho_2 \equiv \frac{m_2}{2\pi T m_0^2} = \frac{\partial_\tau^2 \tilde{\Lambda}}{2\pi \tilde{\Lambda}^2} \Big|_{\tau=\beta/2} \quad (\text{S9})$$

To illustrate the usefulness of this definition, consider the simple case in which  $\sigma'(\omega)$  is a Lorentzian,

$$\sigma'(\omega, T) = \frac{1}{\rho} \left[ \frac{\Gamma^2}{\omega^2 + \Gamma^2} \right] \rightarrow \frac{\rho_2}{\rho} = \frac{2\pi^2 - \beta\Gamma F(\beta\Gamma)}{[F(\beta\Gamma)]^2} \quad (\text{S10})$$

where

$$F(x) = 2x \left[ \psi\left(\frac{x}{2\pi}\right) - \psi\left(\frac{x}{4\pi}\right) - \log(2) \right] - 2\pi, \quad (\text{S11})$$

and  $\psi(x)$  is the digamma function. It is easy to see that  $\rho_2/\rho$  does not depend very strongly on  $\beta\Gamma$ . Specifically,  $\rho_2 \rightarrow \rho$  as  $\beta\Gamma \rightarrow \infty$  and  $\rho_2 \rightarrow \rho/2$  as  $\beta\Gamma \rightarrow 0$  (*i.e.* for a narrow Lorentzian).

Naturally, especially at criticality, it is not reasonable to expect  $\sigma'(\omega)$  to have a simple Lorentzian form. However,  $\rho_2$  turns out to provide a reasonable estimate of  $\rho$  under much more general circumstances. Specifically, let us assume that

$$\sigma'(\omega, T) = \sigma_D(\omega, T) + \sigma_{\text{reg}}(\omega, T), \quad (\text{S12})$$

where  $\sigma_D(\omega, T)$  is a Drude-like piece (*i.e.* maximal at  $\omega = 0$ ), that satisfies

$$\sigma_D(\omega, T) \xrightarrow{T \rightarrow 0} D\delta(\omega), \quad (\text{S13})$$

and whose characteristic width at finite temperature is of the order of  $T$  or less, while  $\sigma_{\text{reg}}(\omega, T)$  is a regular piece with a width that is always large compared to  $T$  and correspondingly a magnitude at low frequencies ( $\omega \lesssim T$ ) that is small compared to  $\sigma_D$  (*i.e.*  $\sigma'_D(0, T) \gg \sigma_{\text{reg}}(0, T)$ ). Evidence for the validity of Eq. (S12) in our problem can be seen by comparing  $\Lambda(i\omega_n)$  for different temperatures. This is shown in Fig. S3. For all temperatures,  $\Lambda(i\omega_n)$  has an apparent “jump” from  $\omega_n = 0$  to  $\omega_n > 0$ .  $\Lambda(i\omega_n)$  for different temperatures are seen to approximately lie on a single, nearly temperature-independent curve. Both features can be readily understood from Eq. (S12). The jump at  $\omega_n = 0$  is a consequence of  $\sigma_D(\omega, T)$ , which so long as its width is less than  $2\pi T$  behaves effectively as if it were a delta function at  $\omega_n = 0$ . The fact that finite  $\omega_n$  data from different temperatures lie on a single curve suggests that  $\sigma_{\text{reg}}(\omega, T)$  is not strongly  $T$  dependent over the relevant range of  $T$ .

We are now faced with the task of disentangling  $\sigma_{\text{reg}}(\omega)$  and  $\sigma_D(\omega)$ . The LFMs clearly combine information about both  $\sigma_{\text{reg}}$  and  $\sigma_D$ . Crucially, however, the two contributions *may scale differently with temperature as  $T \rightarrow 0$* . Consider  $\sigma_{\text{reg}}$ : its contribution to the LFMs, to lowest order in  $T$ , is expected to behave as

$$\begin{aligned} m_{0,\text{reg}} &= \beta \int \frac{d\omega}{2\pi} \frac{\omega \left[ \sigma_{\text{reg}}(0) + \frac{1}{2} \partial_\omega^2 \sigma_{\text{reg}}(0) \omega^2 + \dots \right]}{\sinh\left(\frac{\beta\omega}{2}\right)} \sim T + O(T^3), \\ m_{2,\text{reg}} &= \beta \int \frac{d\omega}{2\pi} \frac{\omega^3 \left[ \sigma_{\text{reg}}(0) + \frac{1}{2} \partial_\omega^2 \sigma_{\text{reg}}(0) \omega^2 + \dots \right]}{\sinh\left(\frac{\beta\omega}{2}\right)} \sim T^3 + O(T^5). \end{aligned} \quad (\text{S14})$$

In contrast, assuming  $\sigma_D(\omega)$  has a width of the order of  $T$  or less, its corresponding LFMs will scale differently. If the total weight of  $\sigma_D(\omega)$  has a non-zero limit as  $T \rightarrow 0$ , and if the characteristic width of  $\sigma_D(\omega)$  is much less than  $T$ , we expect

$$m_{0,D} = \beta \int \frac{d\omega}{2\pi} \frac{\omega \sigma_D(\omega)}{\sinh\left(\frac{\beta\omega}{2}\right)} \approx \int \frac{d\omega}{\pi} \sigma_D(\omega), \quad (\text{S15})$$

and hence, this is non-zero in the  $T \rightarrow 0$  limit. This is true also if the characteristic width of  $\sigma_D(\omega)$  is of the order of  $T$ . For example, if  $\sigma_D$  has a scaling form:  $\sigma_D(\omega, T) = \frac{1}{T} f\left(\frac{\omega}{T}\right)$ , then we get that  $m_{0,D} \rightarrow \int_{-\infty}^{\infty} dx \frac{x f(x)}{2 \sinh\left(\frac{x}{2}\right)} = \text{const.}$  in the limit  $T \rightarrow 0$ . In our data, we find that over a range of temperatures,  $m_0(T)$  is weakly temperature dependent, suggesting that it is dominated by  $m_{0,D}$  (see Fig. S4).

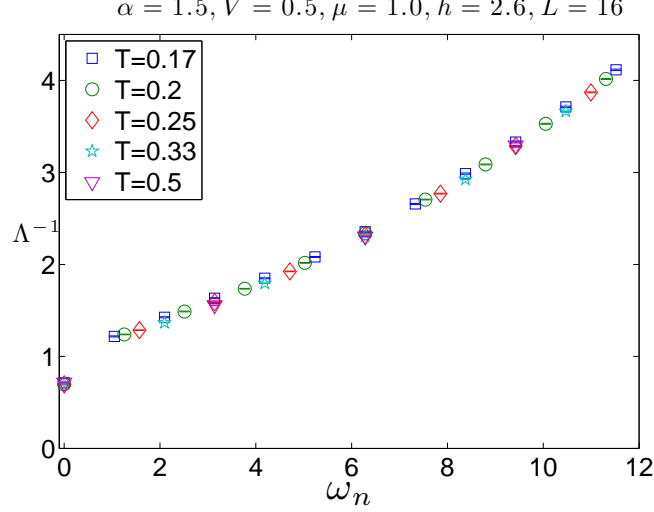


FIG. S3.  $\Lambda^{-1}(i\omega_n)$  at  $h \approx h_c$  for different temperatures. The parameters used in the runs are  $\alpha = 1.5$ ,  $V = 0.5$ ,  $\mu = -1$ , and  $h = 2.6$ .

The interpretation of  $m_2$  is more subtle, as it depends on the precise form of  $\sigma_D(\omega)$  at frequencies of the order of  $T$ . It is instructive to consider a simple model for  $\sigma_D(\omega, T)$ :

$$\sigma_D(\omega, T) = \begin{cases} \sigma_0(T), & \omega < \omega_0(T), \\ \sigma_0(T) \left(\frac{\omega}{\omega_0}\right)^{-\alpha}, & \omega_0(T) < \omega. \end{cases} \quad (\text{S16})$$

with  $\omega_0(T) < AT$ , where  $A$  is a constant. Having a finite optical weight requires  $\alpha > 1$ . Then, to be consistent with the observation that  $m_{0,D} \approx \text{const.}$ , we require that  $\sigma_0(T)\omega_0(T) = D = \text{const.}$  We then get that

$$\begin{aligned} m_{2,D} &\approx \sigma_0(T) \int_0^{\omega_0(T)} d\omega \omega^2 + \sigma_0(T) \int_{\omega_0(T)}^T d\omega \omega^2 \left(\frac{\omega}{\omega_0}\right)^{-\alpha} \\ &= \frac{1}{3} D \omega_0^2 + \frac{1}{3-\alpha} D \omega_0^2 \left[ \left(\frac{T}{\omega_0}\right)^{3-\alpha} - 1 \right]. \end{aligned} \quad (\text{S17})$$

We see that, if  $\omega_0/T \rightarrow 0$  as  $T \rightarrow 0$ , we get that  $m_{2,D}/T^2 \rightarrow 0$  as  $T \rightarrow 0$ . For example, if  $\omega_0 \sim T^{1+\varepsilon}$  with  $\varepsilon > 0$ , then  $m_{2,D} \sim T^{\min[2+(\alpha-1)\varepsilon, 2(1+\varepsilon)]}$ . On the other hand, if  $\omega_0 \sim T$ , we get that  $m_{2,D} \sim T^2$ .

As another example, one can analyze the low-frequency conductivity of a clean Fermi liquid with umklapp scattering. The conductivity is given by

$$\sigma_{\text{FL}}(\omega) = \frac{D}{\pi} \frac{\Gamma_{\text{tr}}(T, \omega)}{[\Gamma_{\text{tr}}(T, \omega)]^2 + \omega^2}, \quad (\text{S18})$$

where the Fermi liquid transport scattering rate is  $\Gamma_{\text{tr}}(T, \omega) = (\omega^2 + 4\pi^2 T^2)/W$  ( $W$  is of the order of the Fermi energy). The integral for  $m_0$  can be calculated in the limit  $T \rightarrow 0$ , and gives  $m_0 = D$ . The integral for  $m_2$  is dominated by frequencies  $\omega \sim T$ , such that at low temperatures,  $m_2 \sim T^3$ .

Turning to our DQMC data,  $m_0$  and  $m_2$  as a function of temperature at criticality are shown in Fig. S4 for two sets of parameters. We find that both  $m_0$  and  $m_2/T^2$  extrapolate to a non-zero value in the limit  $T \rightarrow 0$ . This implies that these moments are indeed dominated by the contribution of  $\sigma_D$ . For the larger  $T_c$  parameter set (right panel), both quantities show a sudden drop at temperatures below  $T = 0.2t$ ; this is likely to be an effect of superconducting fluctuations upon approaching the superconducting critical temperature,  $T_c \approx 0.11t$ . Over a range of temperatures above  $T = 0.05t$  (left panel) and  $T = 0.2t$  (right panel), the observed behavior is consistent with  $\omega_0 \propto T$  in Eq. (S16) and with  $\sigma_0 \propto 1/T$ .

It is worth noting that there are other possible ways to define a resistivity proxy in terms of  $m_0$  and  $m_2$ , depending on the assumed form of  $\sigma$  at criticality. For instance, if  $\sigma_D(\omega) = \sigma_0 g(\frac{\omega}{T})$ , where  $g(x)$  is a dimensionless function with

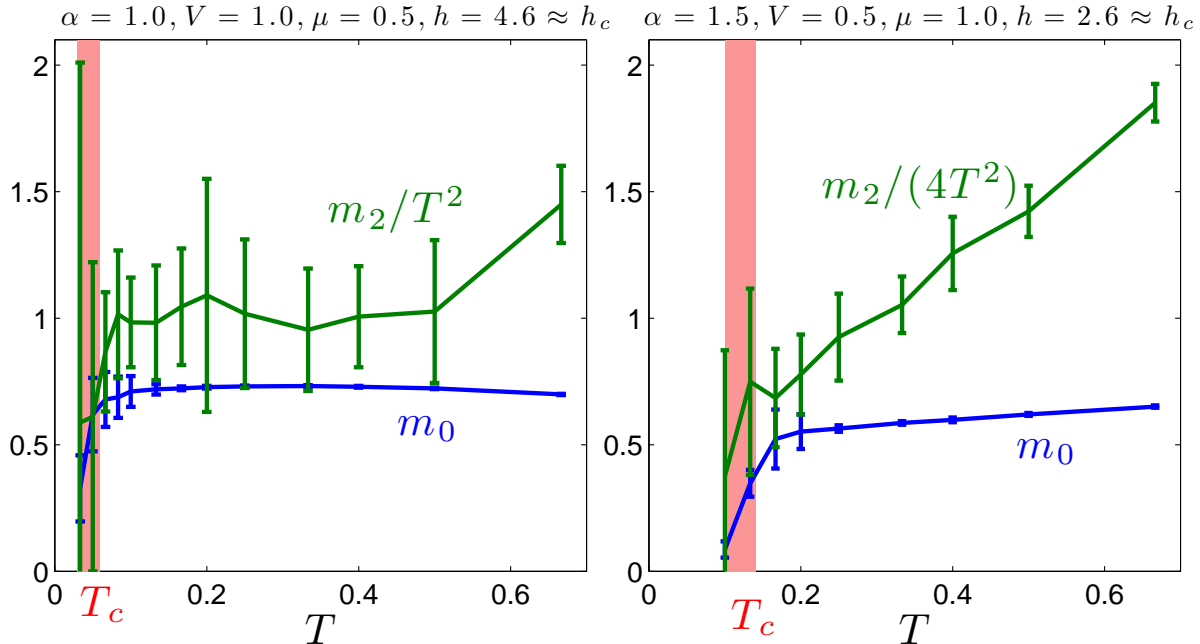


FIG. S4.  $m_0$  and  $m_2/T^2$  as a function of  $T$  at criticality.

a well-defined second moment (unlike a Lorentzian) and  $\Gamma \leq AT$ , we get that  $m_0 \propto \sigma_0 \Gamma$  and  $m_2 \propto \sigma_0 \Gamma^3$ . In this case, a more appropriate resistivity proxy is

$$\tilde{\rho}_2 = \frac{\sqrt{m_2/m_0}}{m_0} \propto \frac{1}{\sigma_0}. \quad (\text{S19})$$

In the particular case where  $\Gamma \propto T$ ,  $\sigma_0 \propto 1/T$ , both  $\rho_2$  and  $\tilde{\rho}_2$  are proportional to  $T$ . Reassuringly, computing  $\tilde{\rho}_2$  from our DQMC data at criticality produces qualitatively similar results as  $\rho_2$ .

### B. Fitting function for $\Lambda(\omega_n)$

In order to fit the imaginary-time data for the current-current correlator,  $\Lambda(\omega_n)$ , we use the following model for the optical conductivity [Eq. (4) of the main text]:

$$\Lambda_{\text{fit}}(\omega_n) = \sum_{j=1}^N \frac{A_j}{\omega_n^2 + \gamma_j |\omega_n| + \Omega_j^2}, \quad (\text{S20})$$

with free parameters  $A_j$ ,  $\gamma_j$ ,  $\Omega_j$ , and we have found that  $N = 2$  is sufficient to fit our data. When comparing this form to the QMC data, we need to recall that the QMC simulations are performed with a finite imaginary time step,  $\Delta\tau$ . The imaginary time correlation function  $\tilde{\Lambda}(\tau)$  is sampled at discrete values  $\tau = n\Delta\tau$  (where  $n$  is an integer), and  $\Lambda(\omega_n)$  is its discrete Fourier transform. In particular,  $\Lambda(\omega_n)$  is periodic in  $\omega_n$  with a period of  $2\pi/\Delta\tau$ . The discrete imaginary time version of (S20), which is appropriate for comparison with our Matsubara frequency data, is

$$\Lambda_{\text{fit},\Delta\tau}(\omega_n) = \sum_{j=1}^N \sum_{q=-\infty}^{\infty} \frac{A_j}{(\omega_n - \frac{2\pi q}{\Delta\tau})^2 + \gamma_j |\omega_n - \frac{2\pi q}{\Delta\tau}| + \Omega_j^2}. \quad (\text{S21})$$

The sum over  $q$  can be performed explicitly, using

$$\sum_{q=-\infty}^{\infty} \frac{1}{(x+q)^2 + A|x+q| + B^2} = \frac{\psi\left(\frac{A}{2} + \frac{\sqrt{A^2-4B^2}}{2} + x\right) - \psi\left(\frac{A}{2} - \frac{\sqrt{A^2-4B^2}}{2} + x\right)}{\sqrt{A^2-4B^2}} + \frac{\psi\left(1 + \frac{A}{2} + \frac{\sqrt{A^2-4B^2}}{2} - x\right) - \psi\left(1 + \frac{A}{2} - \frac{\sqrt{A^2-4B^2}}{2} - x\right)}{\sqrt{A^2-4B^2}}, \quad (\text{S22})$$

where  $\psi(x)$  is a polygamma function,  $A = \frac{\gamma_j \Delta\tau}{2\pi}$ ,  $B = \frac{\Omega_j \Delta\tau}{2\pi}$ , and  $x = \frac{\omega_n \Delta\tau}{2\pi}$  ( $0 \leq x < 1$ ). This is the form we used in our fits to the QMC data.

### C. Sources of error for transport measurements

$$\alpha = 1.0, V = 1.0, \mu = 0.5, h = 4.6 \approx h_c$$

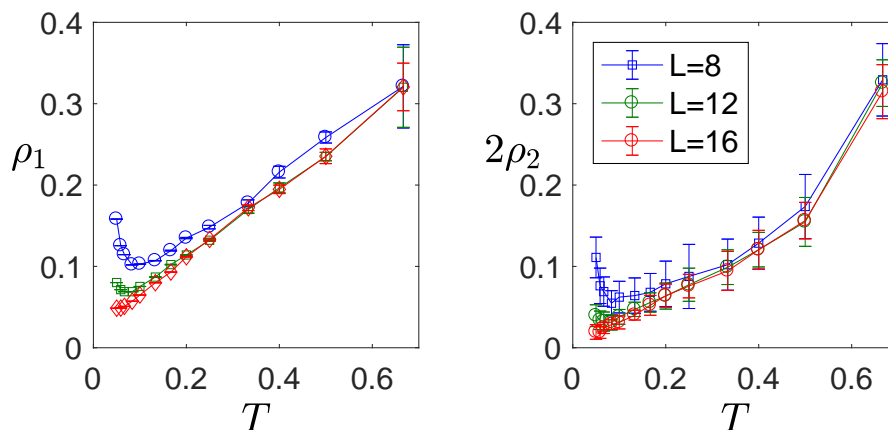


FIG. S5. The temperature dependence of  $\rho_1$  and  $\rho_2$  for various system sizes, including error estimates.

Our numerical experiments entail several sources of error, particularly with respect to measurement of the DC resistivity via  $\rho_1$  and  $\rho_2$ . In this appendix we first discuss error estimates for the finite size data shown in Fig. S5, and then estimate the error entailed by taking the largest available system to represent the thermodynamic limit.

$\rho_2$  is extracted directly from the value and second  $\tau$  derivative of  $\tilde{\Lambda}(\tau)$  at  $\tau = \beta/2$ , which are in turn determined by a linear fit of  $\tilde{\Lambda}(\tau)$  vs  $(\tau - \beta/2)^2$  over an appropriate window. The statistical errors on  $\tilde{\Lambda}(\tau)$  give rise to straightforward confidence intervals on  $\tilde{\Lambda}(\beta/2)$  and  $\partial_\tau^2 \tilde{\Lambda}(\beta/2)$ , which are propagated to yield the error estimates for  $\rho_2$  reflected in Fig. S5.

Fig. S6 shows that statistical error is not a meaningful source of error for  $\rho_1$ . While the two component fit described in the text is consistently within a few percent of  $\Lambda(\omega_n)$ , the deviation substantially exceeds the statistical error bars on  $\Lambda(\omega_n)$  in a systematic, frequency dependent way. It is beyond our simple approach to estimate the magnitude of the error in  $\rho_1$  that this systematic deviation entails. An additional source of error is in numerical minimization—different starting guesses for the least squares algorithm lead to variation of the inferred  $\rho_1$  due to a broad minimum in the objective function, particularly at high temperature. This variation (for several choices of starting guess) yields the error bars pictured in Fig. S5.

For both  $\rho_1$  and  $\rho_2$ , there are systematic finite-size errors that become increasingly important at low temperature. In the text, we quote the value for the largest system size simulated (between  $16 \times 16$  and  $20 \times 20$ , depending on the temperature). To estimate the magnitude of the finite-size error, we perform a quadratic fit to the data as a function of  $1/L$ , as shown in Fig. S7. The difference between the  $1/L \rightarrow 0$  extrapolation and the value for the largest system size is our estimate for the finite size error. The finite size error and the fitting/minimization error are added



$$\alpha = 1.0, V = 1.0, \mu = 0.5, h = 4.6 \approx h_c, \beta = 10, L = 16$$

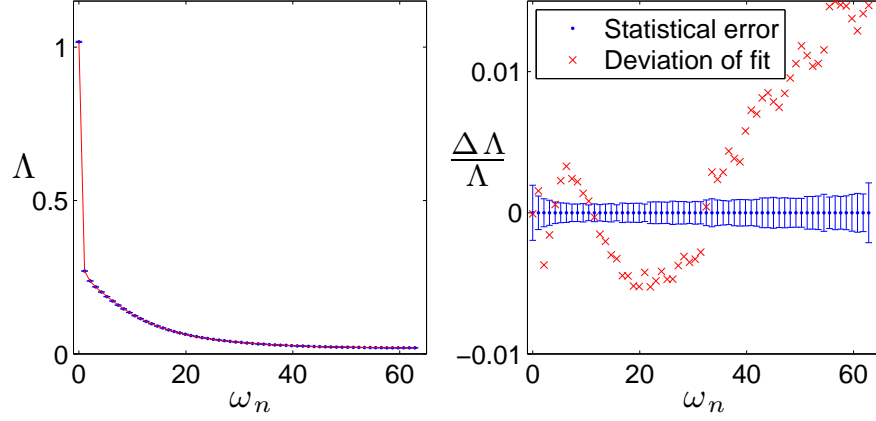


FIG. S6. Left: data for  $\Lambda(\omega_n)$  and the two-component fit described in the text. Right: the deviation between fit and data, expressed as a fraction of  $\Lambda$ , with statistical errors for comparison.

$$\alpha = 1.0, V = 1.0, \mu = 0.5, h = 4.6 \approx h_c, \beta = 10$$

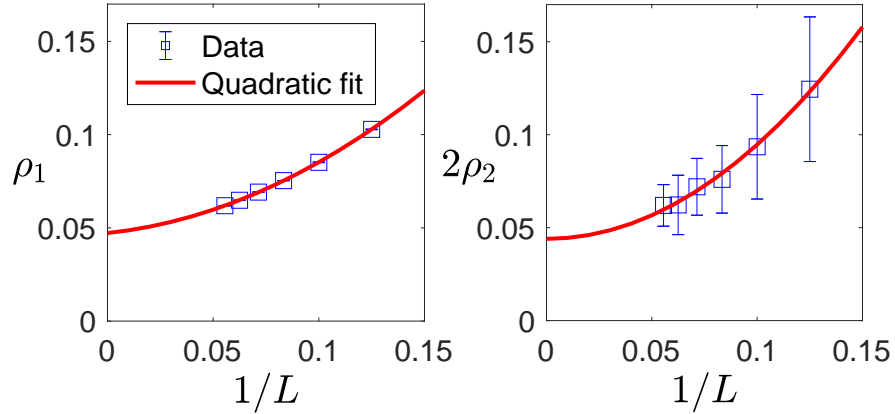


FIG. S7. Estimation of finite size error via a quadratic fit in  $1/L$ .

in quadrature to produce the error estimates in the paper. An identical procedure of error estimation is employed for the width and weight of the Drude-like piece shown in the paper.

#### D. Insensitivity of the fit to an additional narrow peak in $\sigma'(\omega)$

In the main text, we have used a simple two-component form for the conductivity  $\sigma'(\omega)$  to fit the Matsubara frequency data. This is the “minimal” form that is required, in the sense that the data cannot be well described with a single component form. However, as we now show, we cannot exclude the presence of *additional* components. In particular, the data can be described equally well with an additional narrow peak in  $\sigma'(\omega)$  centered at  $\omega = 0$ , whose width is much smaller than  $T$ .

In order to demonstrate this, we have repeated the fitting analysis describes in the paper with an additional

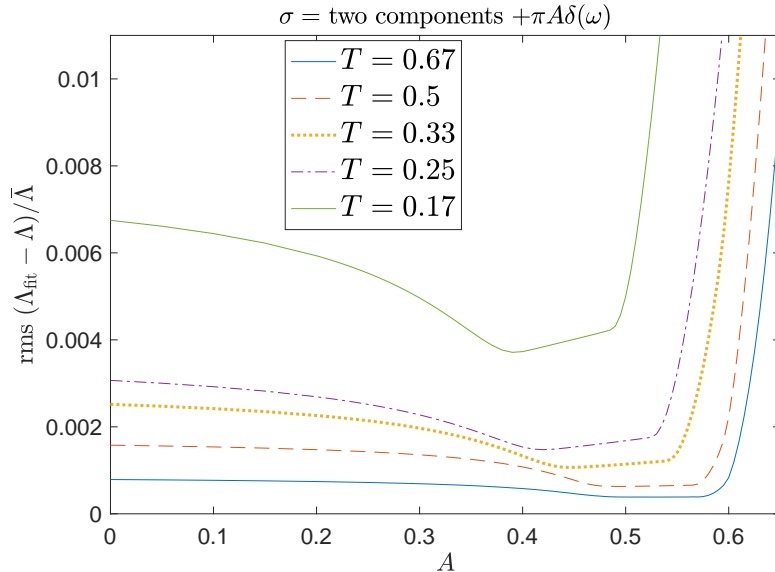


FIG. S8. Softness of the two component conductivity fit to the addition of a sharp Drude peak. Plotted is the root mean squared deviation of the fit from the numerical data, normalized by  $\bar{\Lambda}$ , the mean value of  $\Lambda$ . The parameters used in the QMC run were  $\alpha = 1.5$ ,  $V = 0.5$ ,  $\mu = 1$ ,  $h = 2.6 \approx h_c$ , and  $L = 20$ . The quality of the fit is modestly improved by the addition of a delta function component of fixed weight, with the remaining two components of form (4). As expected, we cannot rule out additional structure of the conductivity at frequencies far less than the temperature.

delta-function contribution to  $\sigma'(\omega)$  with a variable weight  $A$ . This corresponds to the following fitting function:

$$\tilde{\Lambda}_{\text{fit}} = \Lambda_{\text{fit}} + \pi A \delta_{\omega_n, 0}, \quad (\text{S23})$$

where  $\Lambda_{\text{fit}}$  is the two component form used in the main text [Eq. (4) above]. In Fig. S8 we present the root mean square deviation of the best fit as a function of  $A$ . As seen in the figure, the fit quality improves slightly upon increasing  $A$ , until it reaches a certain critical value where the deviation turns up sharply. We conclude that our analysis of the conductivity cannot rule out the presence of additional “fine structure” of  $\sigma'(\omega)$  at frequencies  $\omega \lesssim T$ . In particular, if such fine structure is present, the resistivity proxies can be dramatically different from the true DC resistivity. (For example, if  $A \neq 0$ , the DC resistivity is zero.)

Therefore, the resistivity proxies which we obtained by analyzing the imaginary time (or Matsubara frequency) correlator cannot be related to the true DC resistivity without further assumptions. The proxies can tell us about the DC resistivity only if  $\sigma'(\omega)$  has a sufficiently simple structure at low frequency, such as Eq. (S12) above. The appeal of this form is in its simplicity; however, there are well-defined scenarios where it might fail, e.g. due to the emergence of an approximate conserved momentum in the presence of a sharp Fermi surface. Whether this is the case in our problem requires going beyond the present analysis.

### E. Comparison with maximal-entropy analytic continuation

As an additional test on our results, we obtain the conductivity by applying the maximal entropy method (maxEnt), using Bryan’s algorithm [4, 5]. The maxEnt method, while not as constrained as the fitting approach we have used in the main text, is biased towards producing broad, featureless spectral functions. The resulting conductivity  $\sigma(\omega)$ , shown in Fig. S9 has two-peak structure much like the fitting function used in the main text. Close to criticality, the Drude-like peak at  $\omega = 0$  has width comparable to  $T$ , and the resistivity roughly matches the results of the fit,  $\rho_{\text{maxEnt}} \approx \rho_2$ . There is a greater discrepancy between the two component fit and the maximum entropy result far from  $h_c$ . This is consistent with the development of a parametrically sharp Drude peak (i.e. one with width much smaller than  $T$ ), a feature likely to be ill-captured by any unbiased form of analytic continuation.

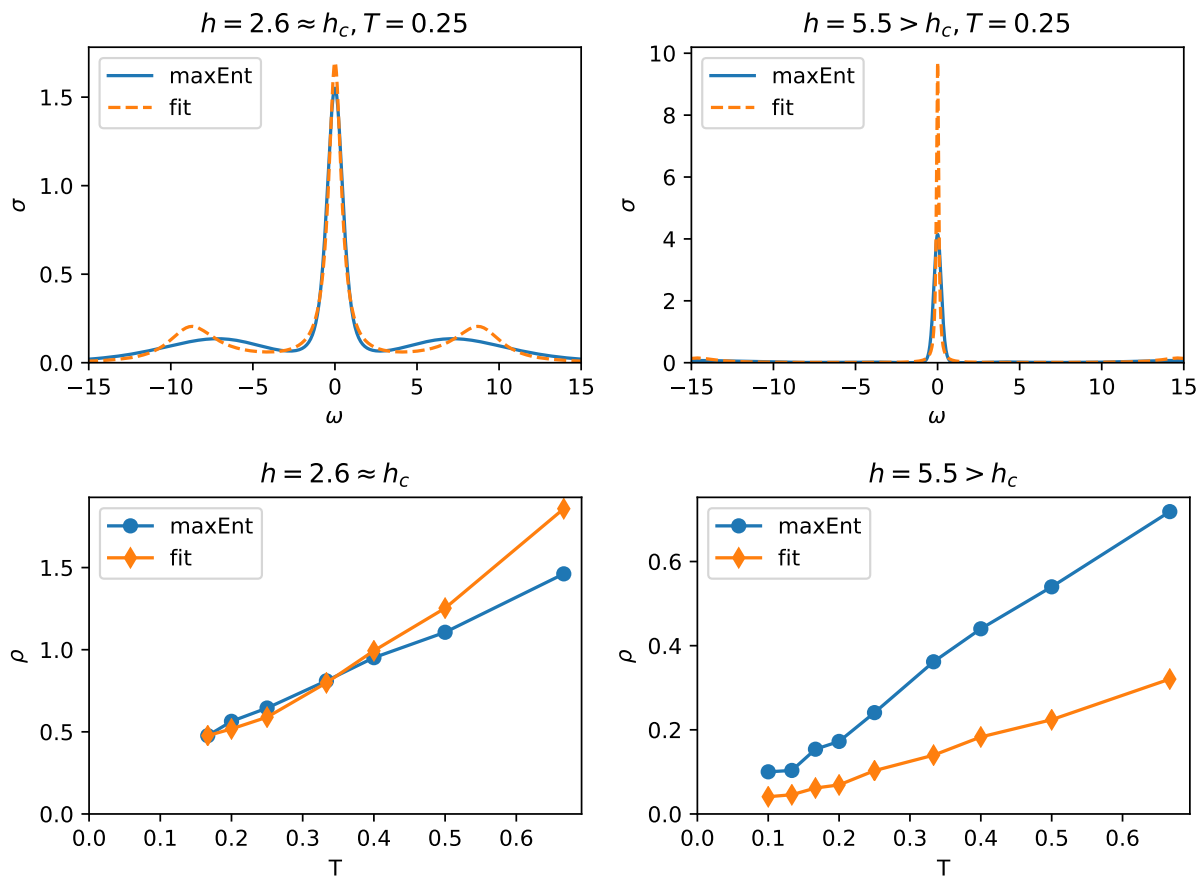


FIG. S9. Top panels: The optical conductivity  $\sigma(\omega)$  as obtained by maxEnt, compared with the fitting function shown in the main text. Bottom panels: The temperature dependence of the DC resistivity obtained by both methods. Shown here for  $\alpha = 1.5, V = 0.5, \mu = 1$

### S-III. FERMION MASS ENHANCEMENT

We present evidence in the main text that the low temperature metallic states for  $h$  away from  $h_c$  are Fermi liquid-like in character, and should therefore be characterized by an effective quasiparticle dispersion. In this section we describe a method to approximately measure this dispersion near the Fermi surface, and show that it is subject to substantial flattening as  $h \rightarrow h_c$ . This reduction in the effective Fermi velocity, which is observed everywhere on the Fermi surface except the cold spots, is typically described as an enhanced effective mass.

We define a low-frequency moment of the spectral function,  $\Omega_1(\vec{k})$  from the Fermion green function  $\tilde{G}(\vec{k}, \tau)$  according to

$$\Omega_1(\vec{k}) = -\partial_\tau \log [\tilde{G}(\vec{k}, \tau)] \Big|_{\tau=\beta/2} = \frac{\int d\omega \frac{\omega A(\vec{k}, \omega)}{\cosh(\beta\omega/2)}}{\int d\omega \frac{A(\vec{k}, \omega)}{\cosh(\beta\omega/2)}}, \quad (\text{S24})$$

where the final equality is an exact identity. For a free fermion system,  $\Omega_1(\vec{k})$  precisely equals the dispersion. In a Fermi liquid at temperature  $T$ , there is a renormalized quasiparticle dispersion  $\epsilon(\vec{k})$ , and as  $\vec{k}$  approaches the Fermi surfaces, the spectral function is dominated by a peak centered at  $\epsilon(\vec{k})$ , with width much less than  $T$ . Accordingly,  $\Omega_1(\vec{k}) \rightarrow \epsilon(\vec{k})$  as  $\epsilon(\vec{k})/T \rightarrow 0$ . Therefore, in a Fermi liquid,  $\Omega_1(\vec{k})$  is a valid proxy for the dispersion within a range  $\sim T$  of the Fermi level. The assumptions above clearly break down close to criticality (at least away from the cold regions), where there are no well-defined quasiparticles.

In Fig. S10 we exhibit the momentum dependence of  $\Omega_1$  at fixed temperature for a variety of values of the tuning parameter  $h$ . Except for near the cold spots,  $\Omega_1$  tends to flatten near the Fermi level as  $h_c$  is approached. Similar results are found for smaller values of the coupling constant and the fermion density.

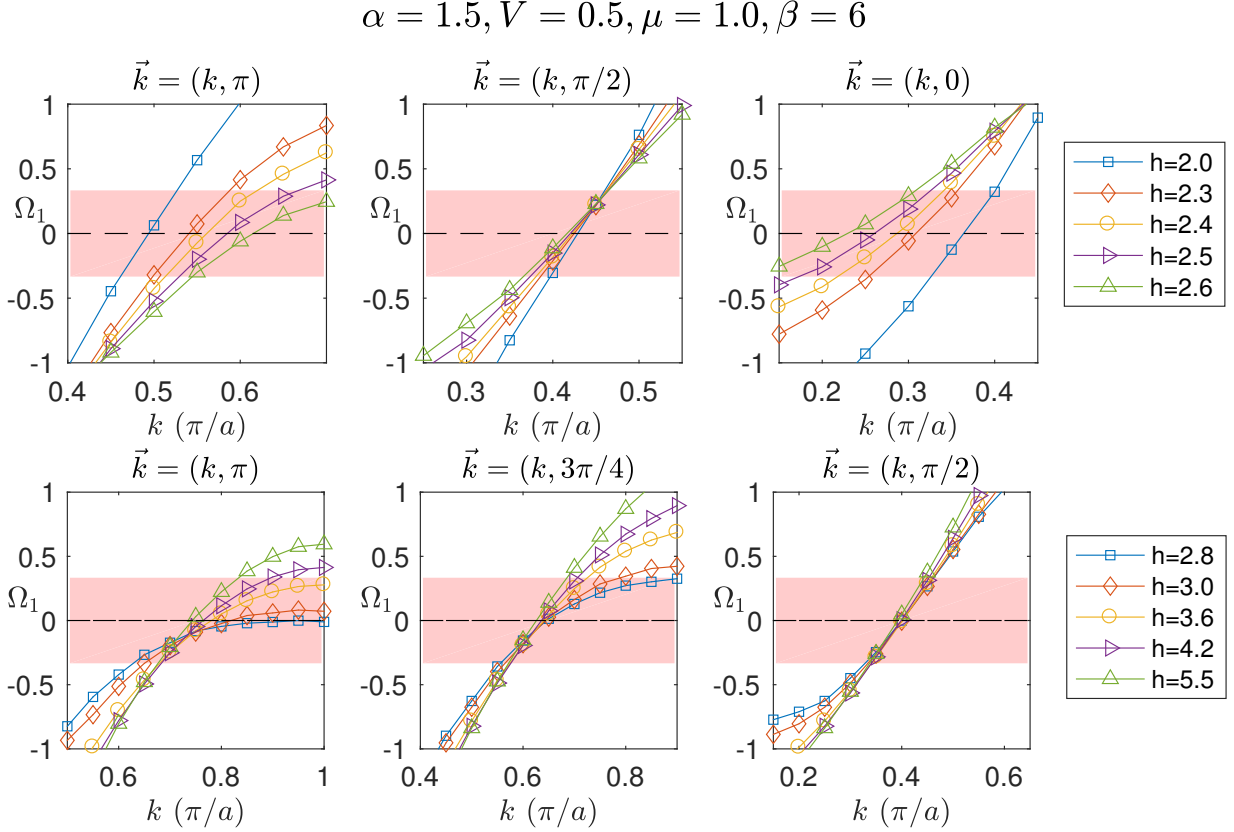


FIG. S10. The low frequency moment  $\Omega_1$  along various cuts through the Fermi surface, showing mass enhancement on approach to the QCP. The QCP is located at  $h \approx 2.6$ , and for  $h \leq h_c$  (upper row), a small symmetry breaking field has been applied to orient the nematic order so that hopping in the  $x$  direction is enhanced (this also cuts off fluctuation effects to some extent near  $h_c$ ). The cut through  $k_y = \pi/2$  passes near the cold spot, and has little mass enhancement on approach to the QCP. The shaded range is within  $2T$  of the Fermi level, roughly where  $\Omega_1$  should faithfully measure the quasiparticle dispersion.

#### S-IV. FERMION SPECTRAL FUNCTION

In this section we construct the fermionic spectral function  $A_{\mathbf{k}}(\omega)$  by the maximum entropy method. Close to criticality, [Fig.S11], the spectral function away from the cold spots shows very broad features, without a well-defined dispersing peak. Below the superconducting  $T_c$ , a gap opens around  $\omega = 0$ . At the cold spots or away from criticality [Fig.S12], we find well-defined peaks, showing a BCS-like transition into the superconducting phase. Although the maxEnt results are visually appealing and agree with the direct analysis of imaginary-time data shown in the main text, a word of caution is in order. The maxEnt method favors spectral functions which are as smooth and featureless as possible, while still in agreement with the data. Thus, it is not reliable for extracting spectral features with typical frequencies much smaller than the temperature.

#### S-V. BEHAVIOR AT LOWER DENSITIES

In this section we present results for somewhat smaller densities than those presented in the main text. We focus on the two sets of couplings  $\alpha$  and  $V$  as in the main text, with the chemical potential set to  $\mu = -2$ . In figure S13 we show the phase diagrams. For both couplings, the finite temperature nematic phase boundary  $T_{\text{nematic}}(h)$  is linear

$$\alpha = 1.5, V = 0.5, \mu = 1, h = 2.6$$

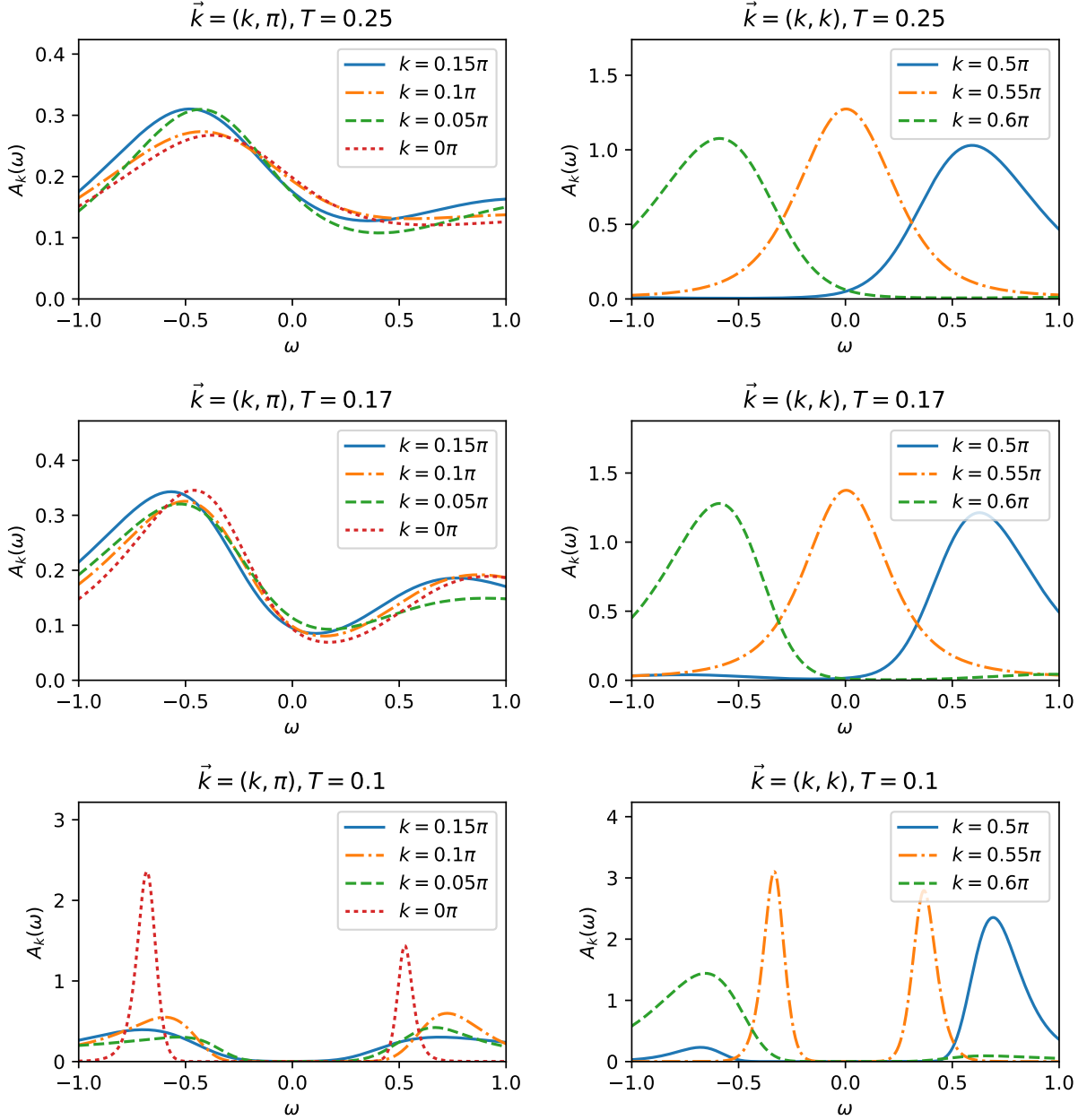


FIG. S11. The fermionic spectral function as obtained by the maxEnt method. Different curves represent different momenta close to the Fermi surface. Shown here for  $h \approx h_c$

at high temperature, and undergoes a sharp change of slope at lower temperatures. At the weaker coupling,  $\alpha = 1$ , a multi-peak structure is seen in the distribution of several thermodynamic quantities, such as the density and the nematic order parameter (not shown), suggesting a weakly first order transition at low temperatures. Whereas at the stronger coupling,  $\alpha = 1.5$  and  $V = 0.5$ , we find a high  $T_c$  superconducting dome with maximal  $T_c \approx 0.12$ , there is no evidence of superconductivity for the weaker coupling,  $\alpha = 1$  and  $V = 1$ , down to temperatures  $T = 0.033$ .

The imaginary part of the single fermion self-energy, shown in Fig. S14, shares similar characteristics to the larger-density data. A substantial “nodal-antinodal” dichotomy is seen, and the self energy close to  $h = h_c$  seems to approach a constant as  $\nu_n \rightarrow 0$ . At the stronger coupling,  $\alpha = 1.5$ , the characteristic upturn of the self energy at low frequencies is seen below the superconducting  $T_c$ .



$$\alpha = 1.5, V = 0.5, \mu = 1, h = 5.5$$

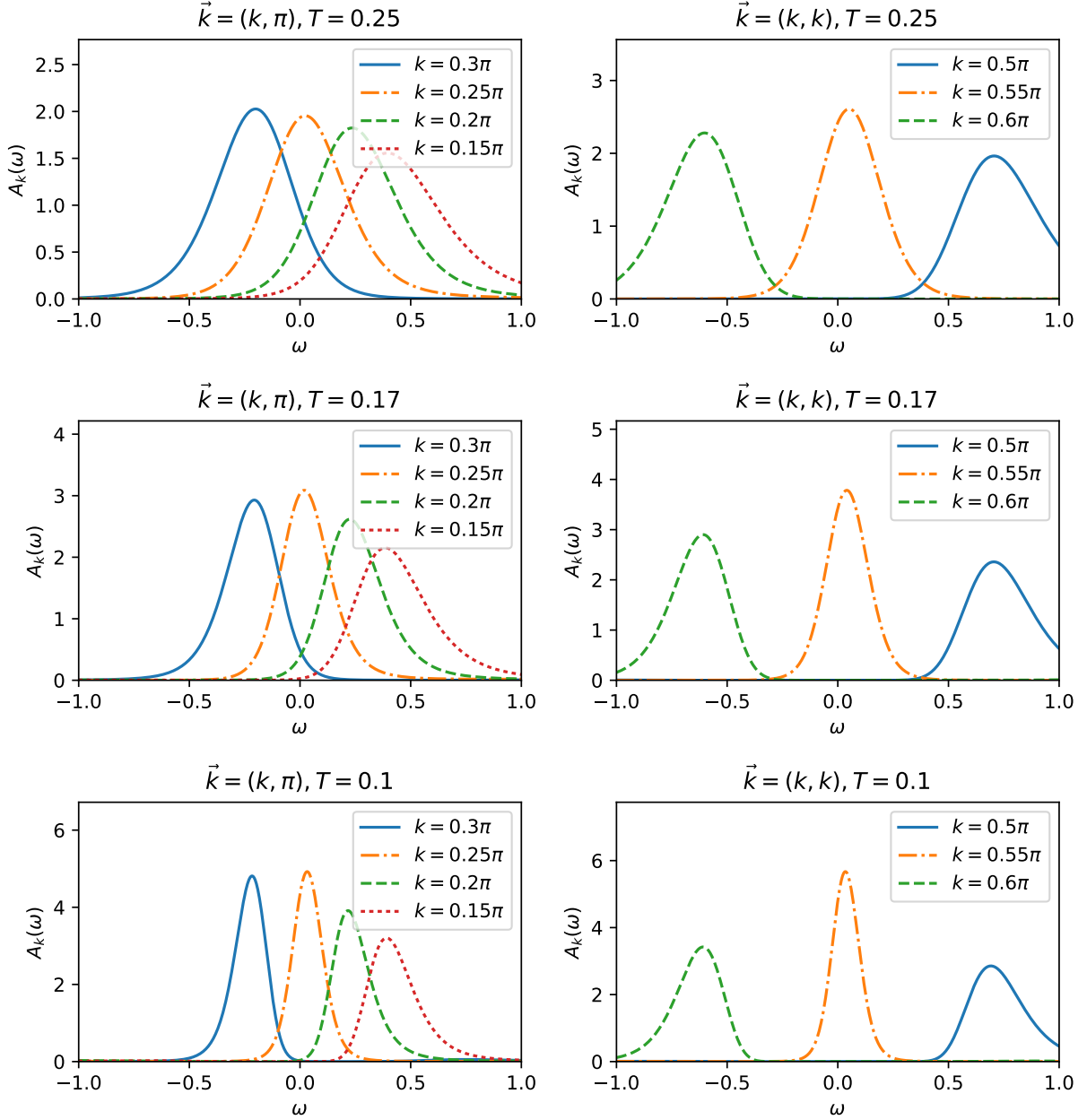


FIG. S12. The fermionic spectral function as obtained by the maxEnt method. Different curves represent different momenta close to the Fermi surface. Shown here for  $h > h_c$

The estimates for the resistivity,  $\rho_1$  and  $\rho_2$ , are shown in Fig. S15. As in the higher densities shown in the main text, the resistivity proxy  $\rho_2$  (right column) agrees qualitatively with the results of the two-component fit  $\rho_1$  (left column). The optical conductivity (not shown) contains a Drude-like peak. The magnitude of the DC resistivity is of order of the quantum of resistance  $\hbar/e^2$ . However, unlike for higher densities, we do not find linear-in  $T$  resistivity over a range of temperatures close to the nematic quantum phase transition.

A possible cause for the qualitative difference in the resistivity between the lower and higher density systems is the smaller size of the Fermi surface at these densities, which might lead to a suppression of certain umklapp processes at low temperatures. For our Fermi surface, an umklapp scattering process involving two fermions near the Fermi point along the line  $(0, \pi) - (\pi, \pi)$ ,  $\vec{k}_h$ , and symmetry-related points requires  $k_h \geq \frac{\pi}{2}$ . Similarly, a process involving

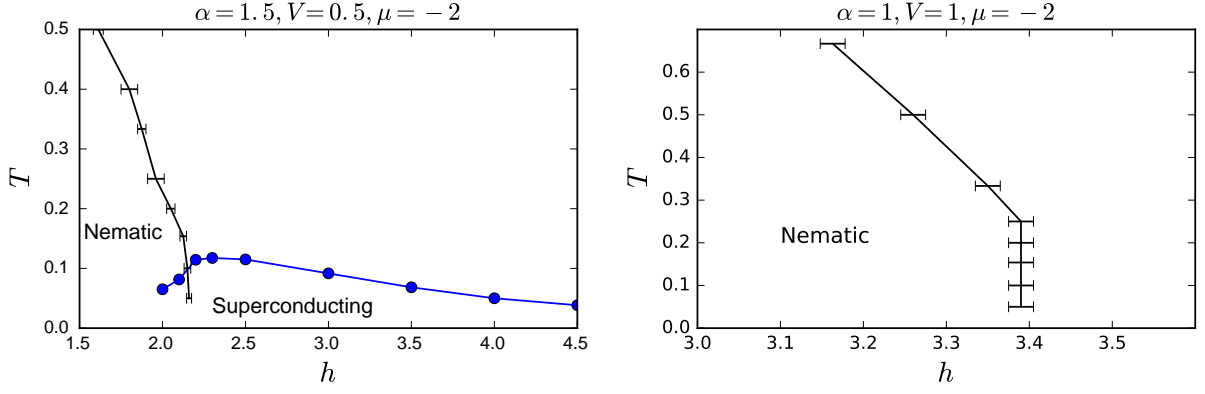


FIG. S13. Phase diagrams for two values of the coupling constants.

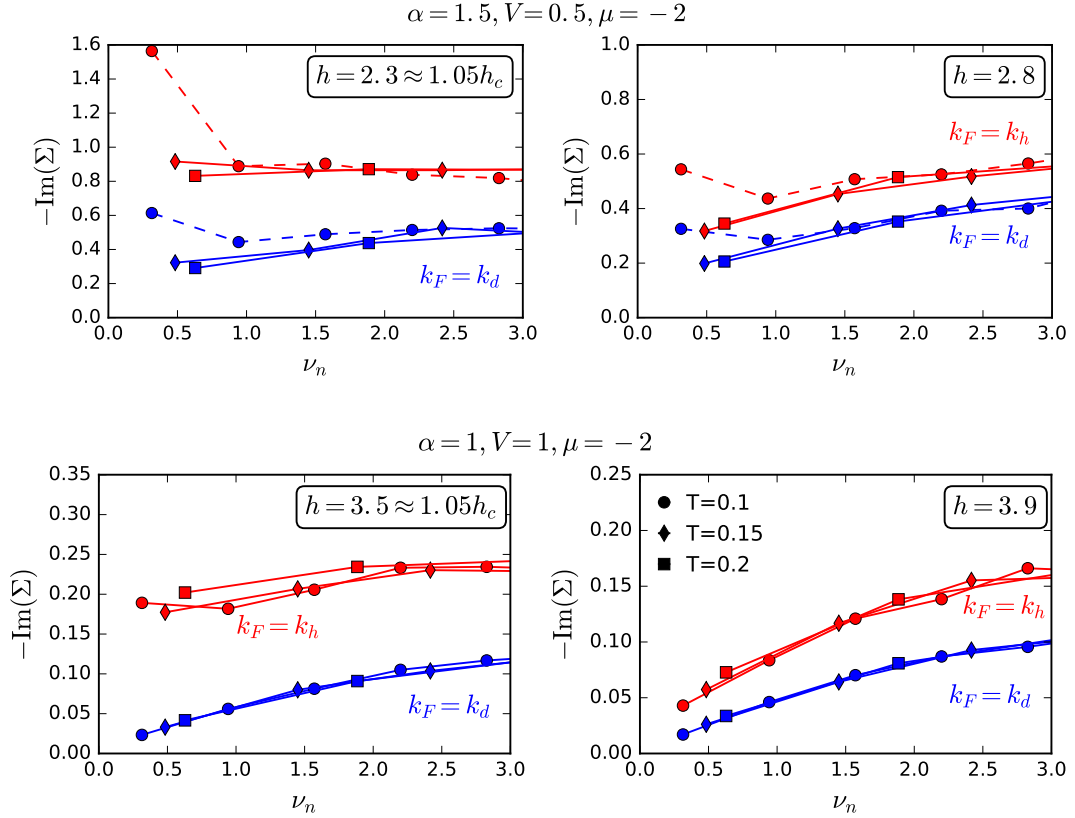


FIG. S14. The imaginary part of the fermion self-energy, for various temperatures and with the nominal Fermi momenta  $k_d$  and  $k_h$  along the  $(0,0) - (\pi, \pi)$  and  $(0, \pi) - (\pi, \pi)$  directions, respectively. Data are shown for a  $14 \times 14$  system both near  $h_c$  (left column) and somewhat in the symmetric phase (right column). In the upper panels, data points below  $T_c$  are connected by dashed lines.

two fermions near the Fermi points along the diagonal,  $\vec{k}_d$ , and symmetry-related points requires  $k_d \geq \frac{\pi}{\sqrt{2}}$ . The magnitudes of the Fermi momenta  $k_d$  and  $k_h$ , measured with respect to  $(\pi, \pi)$ , are shown in Table I, and are found to be close to the aforementioned limiting values.

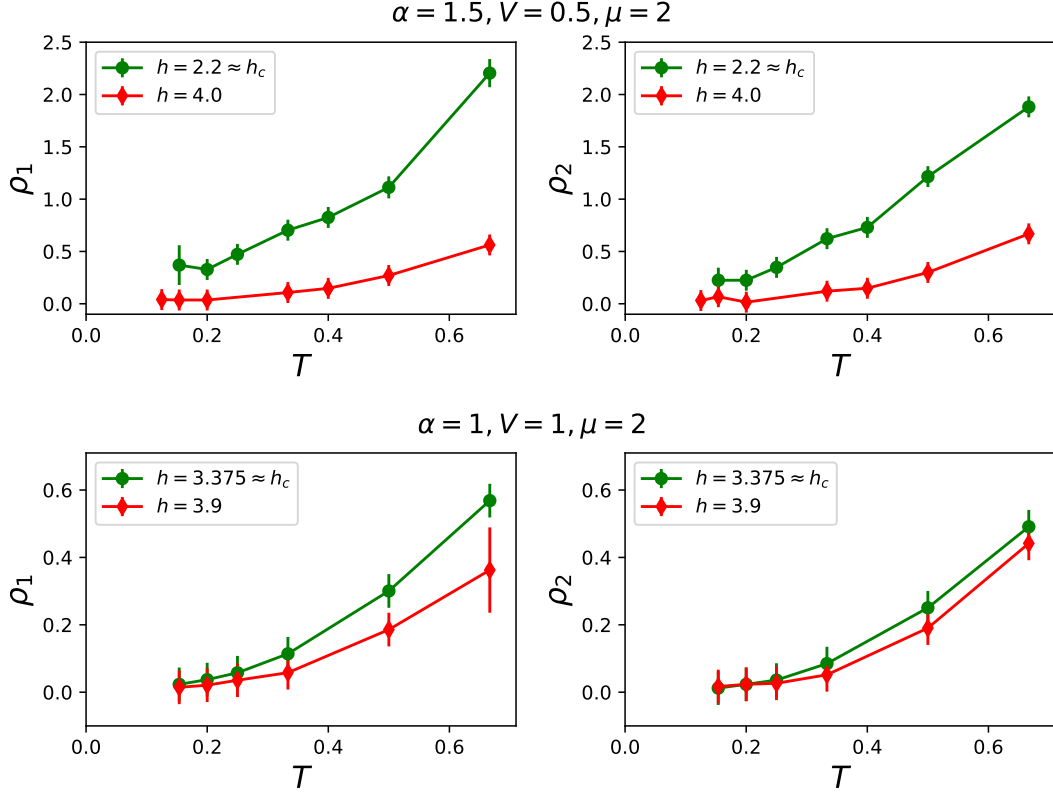


FIG. S15. The temperature dependence of the resistivity.

	$\frac{2k_h}{\pi}$	$\frac{2k_d}{\sqrt{2}\pi}$
$\alpha = 1, V = 1, \mu = -2$	$1.16 \pm 0.08$	$0.72 \pm 0.08$
$\alpha = 1.5, V = 0.5, \mu = -2$	$1.28 \pm 0.08$	$0.80 \pm 0.08$

TABLE I. Magnitudes of Fermi momenta along high symmetry directions.

- 
- [1] Y. Schattner, S. Lederer, S. A. Kivelson, and E. Berg, *Phys. Rev. X* **6**, 031028 (2016).  
[2] T. Paiva, R. R. dos Santos, R. T. Scalettar, and P. J. H. Denteneer, *Phys. Rev. B* **69**, 184501 (2004).  
[3] N. Trivedi and M. Randeria, *Phys. Rev. Lett.* **75**, 312 (1995).  
[4] M. Jarrell and J. Gubernatis, *Physics Reports* **269**, 133 (1996).  
[5] R. K. Bryan, *European Biophysics Journal* **18**, 165 (1990).